NTNU – Trondheim
Norwegian University of
Science and Technology

Mechanical Properties and Corrosion Behaviour of Extruded and Welded AA6082

Kjetil Steen Rostad

Materials Science and Engineering
Submission date: June 2014
Supervisor: Trond Furu, IMTE
Co-supervisor: Otto Lunder, IMT
Kemal Nisancioglu, IMT

Norwegian University of Science and Technology
Department of Materials Science and Engineering

Abstract

Welding and corrosion will play a key role in the further increased use of aluminium alloys in industrial applications. This is especially true as the oil and gas industry is moving into the arctic region in search for new oil and gas reservoirs. The effect on corrosion of the low temperatures that will be encountered in this region must be understood. In this study, six extruded and welded AA6082-T6 flat bars with thicknesses ranging from 10 to 30 mm have been subjected to material characterization, an accelerated intergranular corrosion (IGC) test, recording of polarization curves in artificial seawater at high and low temperatures and measurements of open circuit potential (OCP) at high and low temperatures.

The results from this study show that the extent and weakening of the heat affected zone (HAZ) will not change as the thickness is increased up to 30 mm. Moreover, the HAZ in the examined profiles will not be more susceptible to IGC and pitting corrosion than the base material. It is therefore recommended that the standards on aluminium structures, like EN 1999-1-1[1], include welded aluminium profiles up to 30 mm, as compared to the maximum thickness of 15 mm at present time. Results also show that the corrosion behaviour at low ocean temperatures will be superior compared to higher temperatures. This is shown by the raising of the pitting potential, corrosion potential and OCP at low temperatures, in addition to a lowering of the cathodic limiting current.

Sammendrag

Sveising og korrosjon vil være avgjørende for videre bruk av aluminiumslegeringer i industrielle applikasjoner. Det er spesielt viktig nå som olje- og gassindustrien beveger seg lenger og lenger nordover inn i det arktiske området i søken etter nye olje- og gassfelt. Effekten av de lave temperaturene i disse områdene på korrosjon må forstås. I denne studien er seks ekstruderte og sveiste AA6082-T6 profiler med tykkelse mellom 10 og 30 mm blitt materialkarakterisert, utsatt for en akselerert interkrystallinsk korrosjons (IKK) test, opptak av polariseringskurver i kunstig sjøvann ved høy og lav temperatur og åpen krets potensialmålinger ved høy og lav temperatur.

Resultater fra denne studien viser at utstrekningen og svekkelsen av den varmepåvirkede sonen etter sveising ikke vil variere når platetykkelsen øker opp til 30 mm. I tillegg vil den varmepåvirkede sonen ikke være mer utsatt for IKK og gropkorrosjon enn bulkmaterialet. Det er derfor anbefalt at de rådende standardene for aluminiumsstrukturer, som EN 1999-1-1[1], inkluderer sveisede aluminiumsprofiler med en tykkelse opp til 30 mm, sammenlignet med maksimumstykkelsen på 15 mm på nåværende tidspunkt. Resultatene viser også at korrosjonsmotstanden ved lave havtemperaturer vil være bedre enn ved høyere temperaturer. Dette er vist ved en økning av gropkorrosjonspotensialet, korrosjonspotensialet og åpen krets potensial ved lave temperaturer, i tillegg til en senking av den katodiske grensestrømmen.

Preface

This master thesis has been part of a cooperation between Norwegian University of Science and Technology (NTNU), Hydro Aluminium and Qatar University. The financial support they have offered is appreciated. In particular, the visit to Qatar University and the Qatalum aluminium smelter plant in Doha, Qatar, was much appreciated and led to valuable motivation and knowledge utilized during the work of this thesis.

I would like to give a special thanks to my supervisor adjunct professor Dr. Trond Furu[1] for very encouraging talks about aluminium and guidance. My co-supervisor Dr. Otto Lunder[2] is also acknowledged for valuable help and guidance. Furthermore, I would like to thank Ole Runar Myhr[3] and Terje Iveland[1] for help on weld simulations and Ann Karin Kvernbråten[2] for supplying artificial seawater.

Finally, I would like to offer my gratitude towards Ingrid, Jon Arne, Olise, Gerd, Idar and my fellow students for giving me some much needed moral support.

Trondheim, June 2014

Kjetil Steen Rostad

[1] Hydro Aluminium, Sunndalsøra
[2] SINTEF Material and Chemistry, Trondheim
[3] Hydro Aluminium, Raufoss

Table of Contents

List of Figures

List of Tables

List of Abbreviations

β	Equilibrium phase (Mg_2Si)
β'	Hardening precipitate in AlMgSi alloys (hexagonal semi-coherent needles)
β''	Hardening precipitate in AlMgSi alloys (monoclonal semi-coherent needles)
σ_i	Intrinsic yield strength of pure aluminum (N/m_2)
σ_p	Contribution from hardening precipitates and dispersoids to the overall macroscopic yield strength (N/m_2)
σ_{ss}	Contribution from alloying elements in solid solution to the overall macroscopic yield strength (N/m_2)
AA6082	Aluminium alloy 6082
DBTT	Ductile to brittle transition temperature
E_{corr}	Corrosion potential
E_{pc}	Pitting corrosion potential
FSW	Friction stir welding
GP-zones	Metastable Guinier-Preston zones that precipitate prior to the hardening β' and β'' particles
GTAW	Gas tungsten arc welding
HAZ	Heat affected zone
HV	Vickers hardness
HV1	Vickers hardness – 1 kg load
IGC	Intergranular corrosion
OCP	Open circuit potential
PFZ	Particle free zone
R_m	Yield strength
$R_{p0.2}$	Tensile strength
SSSS	Super saturated solid-solution
T6	Alloy solution-treated and artificially aged to peak strength
TIG	Tungsten inert gas welding
WPS	Welding procedure specification
wt%	Weight percent

1 Introduction

Welding, and its effect on mechanical and corrosion properties, will play a key role in the further use of aluminium in industrial applications. It is well established that the heat affected zone (HAZ) can lose up to 50 % of the strength of the parent material during fusion welding aluminium alloys[2], but the changes in corrosion behaviour for the HAZ and weld material has not received the same amount of attention. Because these alloys possess very attractive properties like low density, ability to be extruded into large and complex shapes, excellent corrosion behaviour, good weldability and no ductile to brittle transition temperature (DBTT) they can prove cost efficient for the offshore oil and gas industry. This is especially true as this industry is moving further north in search for new oil reservoirs. In fact, it is said that 25 % of the world's undiscovered oil and gas is located in the arctic region[3]. Aluminium alloys like AlMgSi may be the answer to how to take advantage of these vast resources in the most cost efficient way.

The oil and gas industry is dependent on good standards and guidelines for aluminium structures, but the ruling standards, like EN 1999-1-1[1], does not allow the use of welded aluminium profiles with a thickness greater than 15 mm[1]. This is because it is believed that the HAZ will be further weakened by multi pass welding for thicker profiles. The use of thicker construction profiles is, however, crucial if aluminium is going to be used in further applications in the oil and gas industry and the aluminium industry must therefore contribute to evaluate and develop these standards. Aluminium is also regarded as more environmentally friendly than other construction materials, due to easy and low energy demanding recycling. This has contributed to that 75 % of all the aluminium ever produced is currently still in use and recycling of aluminium saves over 90 million tons of CO_2 annually[4].

It is commonly believed that the corrosion behaviour will be favorable at low temperatures compared to high temperatures. This is based on studies conducted at room temperature and upwards, but knowing that sea water temperatures as low as 2 °C can be encountered in the arctic region, it is crucial to understand what happens at these temperatures.

Objectives of thesis

In this study, six different profiles of AA6082 with thicknesses ranging from 10 to 30 mm have undergone material characterization and an accelerated intergranular corrosion (IGC) test. As all the examined profiles were extruded and thereby fusion welded, the effect of microstructure and welding on the IGC susceptibility has been evaluated.

Corrosion behaviour at low temperatures has also been studied by recording polarization curves and measuring the open circuit potential at 25 and 2 °C. The polarization curves were recorded in an

electrolyte of artificial seawater and the electrolyte was bubbled with both synthetic air and nitrogen gas to saturate and deplete it with oxygen, respectively. The open circuit potential measurements were recorded over the course of 12 hours where the electrolyte was continually bubbled with synthetic air. Furthermore, weld simulations were carried out to see how multi-pass welding can be correctly simulated regarding strength in the heat affected zone.

This thesis aims to provide some insight to the challenges and possibilities of using aluminium alloys in the arctic region, with regards to welding and corrosion behaviour. It should be mentioned that more studies on the subject is needed, as it is a wide and complex subject.

2 Background

2.1 AlMgSi-alloys

AlMgSi-alloys are extensively used in buildings, transport and engineering throughout the world, mostly as extruded profiles. In 2001, two million tons of extruded AlMgSi-profiles were consumed in western Europe alone[5]. These alloys contains a range of trace and alloying elements, e.g. Fe, Mn, Cu, Cr, Zn, but the main alloying elements are Mg and Si in a range of 0.5-1.3 wt% and 0.4-1.4 wt%, respectively. The main effects of selected alloying elements are summarized in Table 2.2. With respect to local corrosion, the Cu-content and the Mg/Si-ratio has proven to be of upmost importance, and will be reviewed in section 2.5. Given that AlMgSi-alloys get most of their strength from precipitation hardening (section 2.3), the mechanical properties presented in Table 2.1 has a wide range.

Table 2.1: Selected mechanical properties for AlMgSi-alloys[6].

Selected mechanical properties	
$R_{p0.2}$	190-360 MPa
R_m	220-390 MPa
Elongation	12-17%

Table 2.2: Main effect(s) of selected alloying elements in AlMgSi-alloys[6]

Element	**Main effect(s)**
Cr	Grain refiner, hinder recrystallization
Cu	Increase strength
Fe	Contamination, reduce corrosion resistance
Mg	Increase strength, more stable oxide layer
Mn	Grain refiner, hinder recrystallization
Si	Increase strength
Zn	Contamination

In Figure 2.1, a pseudo-binary Al-Mg_2Si phase diagram is presented as calculated by J. Zhang, et al[7]. From the diagram a ternary phase field of liquid+Al+Mg_2Si and a pseudo-eutectic point at Al – 13.9 wt% Mg_2Si can be seen. The maximum solubility of Mg_2Si is 1.9 wt% at 582.5 °C.

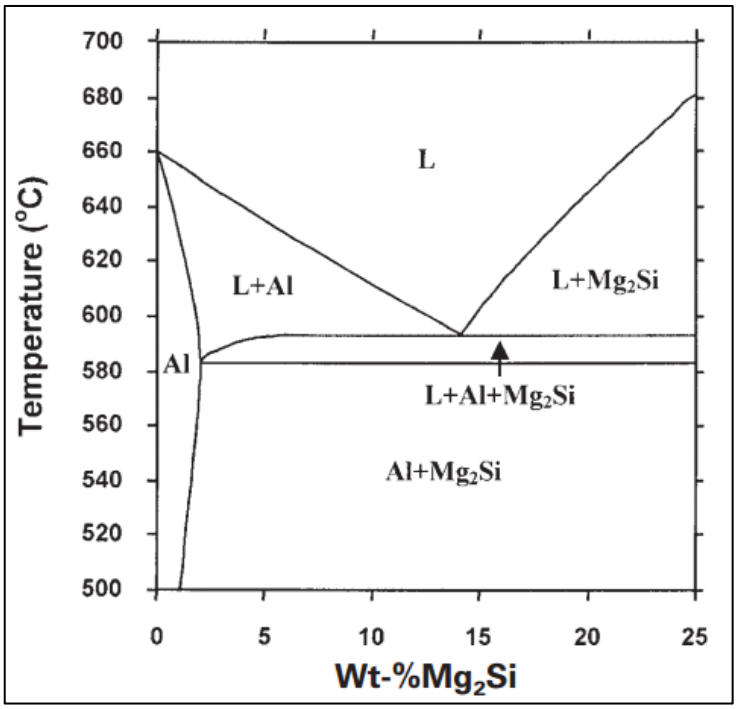

Figure 2.1: Pseudo-binary phase diagram for Al-Mg_2Si[7].

2.2 Extrusion of AlMgSi-alloys

In Figure 2.2 the general production cycle for extruded AlMgSi-alloys is shown together with approximate temperature and times for the individual heat treatments. Casting produces billets with varying diameter and length dependent on the intended use. After casting homogenization is carried out to level out micro segregations, get rid of low melting point eutectics, spheroidize the insoluble phase particles and control the precipitation of dispersoids particles[8].

Prior to extrusion, the billets are preheated to achieve the required formability. During extrusion the grain structure will change dramatically, as depicted in Figure 2.3. Grains will be pressed together and elongated in the direction of extrusion, producing what is called a fibrous microstructure. Towards the outer surface of the resulting profile, deformation and friction will be higher than in the center. This gives higher strain rates and dislocation densities, which again leads to better conditions for recrystallization. A typical extruded profile will have a recrystallized outer surface and a bulk material with a fibrous microstructure. The extent of the recrystallized layer is dependent on many factors, including, but not limited to; particle size, particle strength, extrusion speed, manganese and chromium content and homogenization parameters[5, 8, 9]. After extrusion, artificial ageing is usually carried out to strengthen the material.

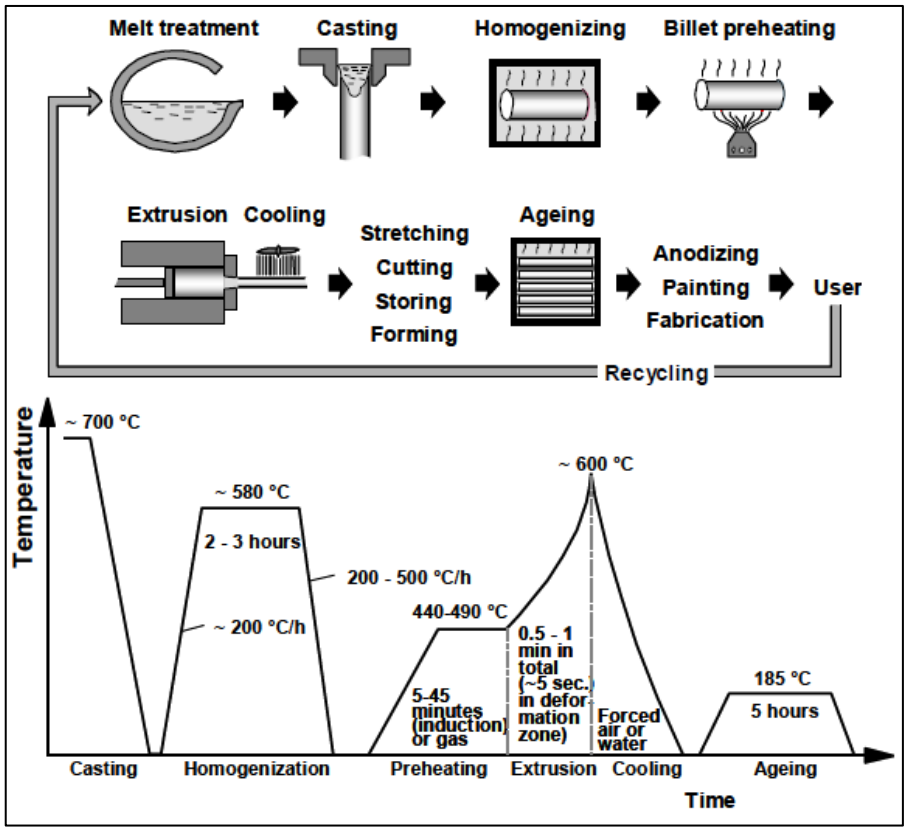

Figure 2.2: Sketch of production cycle for extruded AlMgSi-alloys with approximate temperatures and times for the different heat treatments [5].

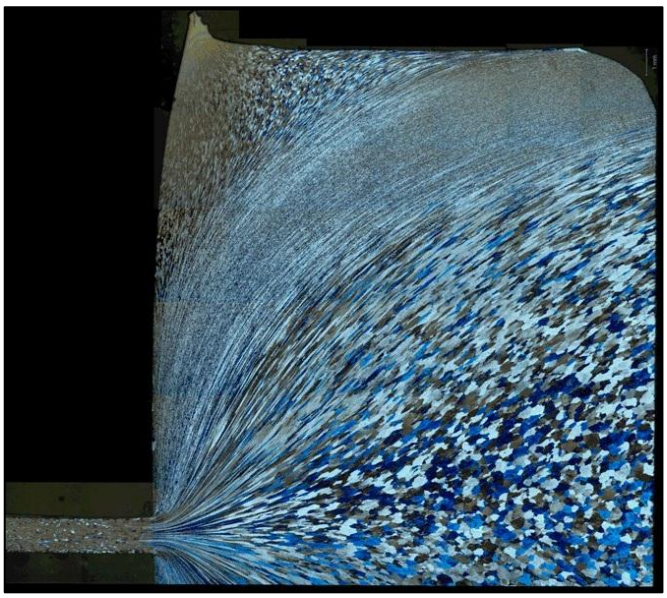

Figure 2.3: Grain structure development during extrusion (printed with permission from Trond Furu)

2.3 Precipitation hardening

It is well known that AlMgSi-alloys get their overall hardness, and hence their yield strength from three different contributions as shown in Equation 2.1.

Equation 2.1: Yield strength for AlMgSi-alloys.

$$\sigma_y = \sigma_i + \sigma_{ss} + \sigma_p$$

Where σ_i is the intrinsic contribution from pure aluminium, σ_{ss} is the contribution from alloying elements in solid solution and σ_p is the contribution from hardening precipitates and dispersoids[10]. The strengthening from elements in solid solution and hardening particles both act by making it harder for dislocations to move. Elements in solid solution do this by creating an elastic stress field around the dissolved element. When a dislocation encounter a particle it can either by-pass it, as is the case for large particles, or shear it, as is the case for small particles[10]. Both these behaviours will make it harder for the dislocation to move and thereby strengthening the material [10-12]. A peak hardness is observed when a mixture of by-passing and shearing particles are present.

Thermal processing in multiple steps is required to control the precipitation of the hardening precipitates. First the alloy is heated to a temperature above the solvus line, but well below the eutectic temperature to avoid local melting, and then quenching to room temperature is performed. This heat treatment will dissolve all the alloying elements in solid solution and will result in a super saturated solid solution (SSSS). After this, artificial ageing is done at temperatures ranging from 150-190 °C. At these temperatures a series of different meta-stable and stable hardening particles will precipitate. The type and order of the precipitates is dependent on several factors including the Cu-content and the Mg/Si-ratio. For a Cu-free, balanced alloy (Mg/Si=1.73 wt%) the precipitation sequence is proposed to be as shown in Equation 2.2. Table 2.3 gives more data on these precipitates.

Equation 2.2: Precipitation sequence for a Cu-free, balanced alloy[13].

$$SSSS \rightarrow atomic\ clusters \rightarrow GP-zones \rightarrow \beta'' \rightarrow \beta',\ \text{U1, U2, B'} \rightarrow \beta / Si$$

Table 2.3: Shape, space group and proposed composition of different hardening precipitates in a Cu-free alloy[6, 13].

Phase	Shape	Space group	Composition
GP-zones	Semi-coherent needles	Monoclinal	$Mg_{2+x}Al_{7-x-y}Si_{2+y}$, $1<x+y<3$
β''	Semi-coherent needles	Monoclinal	Mg_5Si_6
β'	Semi-coherent needles	Hexagonal	$Mg_{1.8}Si$
U1	Needle	Hexagonal	$MgAl_2Si_2$
U2	Needle	Hexagonal	MgAlSi
B'	Lath	Hexagonal	$Mg_9Al_3Si_7$
β	Incoherent plates	Cubic	Mg_2Si

Figure 2.4 shows a sketch of the strength evolution during artificial ageing together with the dominant hardening phases. As can be seen, a peak hardness is achieved when a mixture of β' and β'' is present[14].

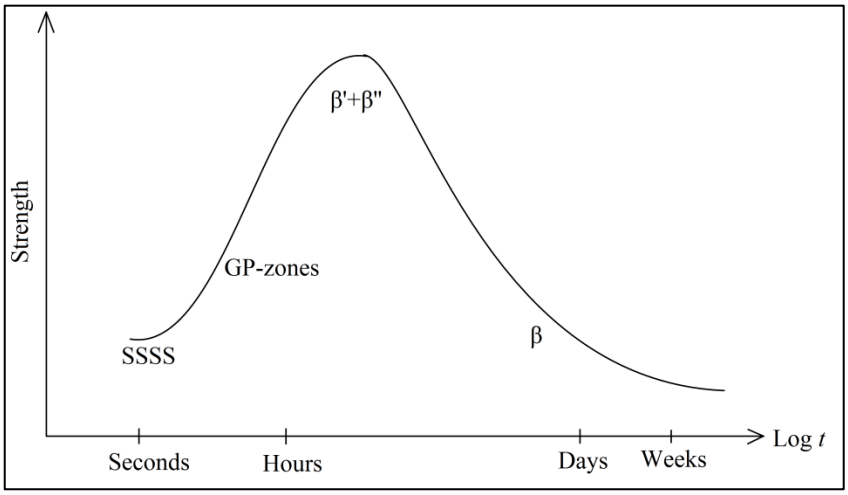

Figure 2.4: Strength evolution during artificial ageing[14].

For a copper-containing alloy the precipitation sequence differs from the Cu-free alloy, as shown in Equation 2.3. The composition of these precipitates are yet to be determined, but there has been some suggestions to the Q' and Q phases, which are believed to be similar. The suggested compositions include $Al_3Mg_9Si_7Cu_2$[15], $Al_5Mg_8Si_6Cu_{2[16]}$, $Al_3Cu_2Mg_9Si_7$[13] and $Al_4Mg_8Si_7Cu_2$[17]. In this study, the latter will be considered. Table 2.4 presents an overview of the accessible data for these precipitates.

Equation 2.3: Precipitation sequence for a Cu-containing alloy[13].

$$SSSS \rightarrow atomic\ clusters \rightarrow GP-zones \rightarrow \beta'',\ L,\ QP,\ QC \rightarrow \beta',\ Q' \rightarrow Q$$

Table 2.4: Shape, space group and proposed composition of different hardening precipitates in a Cu-containing alloy[13, 17].

Phase	Shape	Space group	Composition
QP	Needle	Hexagonal	Unknown
QC	Needle	Hexagonal	Unknown
L	Needle	Unknown	Unknown
Q’	Needle	Probably hexagonal	Uncertain ($Al_4Mg_8Si_7Cu_2$)
Q	Needle	Hexagonal	Uncertain ($Al_4Mg_8Si_7Cu_2$)

2.4 Metal inert gas (MIG) welding of aluminium

Welding is of high importance in industrial applications, and welding of aluminium is generally performed either as fusion welding or solid state welding. During solid state welding heating is performed without any melting taking place, whereas for fusion welding the weld is melted. As the profiles in this study where welded by a type of fusion welding called metal inert gas (MIG) welding, this weld technique will be reviewed in the following.

Figure 2.5 shows the basic principles of MIG welding, or gas metal arc welding (GMAW). This welding technique is widely used in industrial applications and can be used to weld a vast variety of metals. A consumable wire is fed continuously through a nozzle and acts both as filler metal and electrode. When the wire touches the parent metal an arc is established and the wire melts and transfers metal. The transfer mode depends on several variables like wire speed, current mode, wire diameter and shielding gas. The shielding gas protects the arc and the weld pool from oxidation and stabilizes the arc, and often consists of argon, helium, CO_2 or a mixture of argon and CO_2 or argon and helium[18].

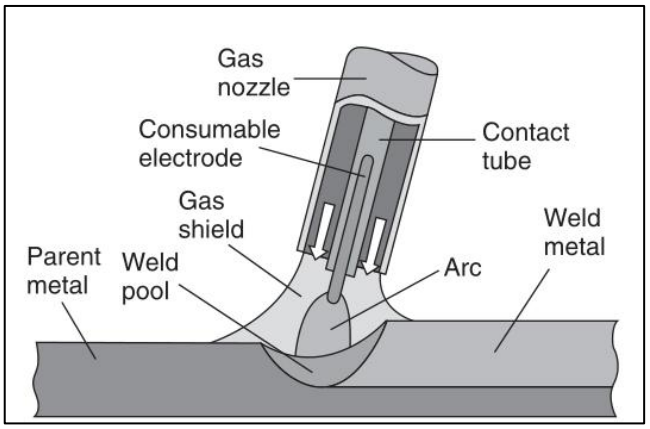

Figure 2.5: Sketch of the basic principles of the gas metal arc welding (GMAW) technique[19].

MIG welding is a versatile welding technique that can be used in all positions, capable of high welding speeds, provides good oxide film removal and fits most geometries[18, 19]. One major drawback of fusion welding of aluminium is that it gives a significant softening of the weld metal and the heat affected zone (HAZ) close to the weld. This issue will be reviewed in some further detail in the following section together with the changes in microstructure.

2.4.1 Microstructure and strength evolution during fusion welding

As mentioned in the previous section, a loss in strength compared to the parent material in the region close to the weld, often referred to as the heat affected zone (HAZ), and the weld metal is a challenge for fusion welding. This loss in strength can be explained by the dissolution and growth of the hardening particles β' and β'' in the HAZ. As the weld will melt during fusion welding, it will upon solidification form an as cast microstructure, with the resulting strength associated with this structure[20].

Grong[14] and Myhr et al.[11] studied the changes in microstructure and strength during fusion welding of AlMgSi-alloys and a simplified overview of these changes is presented in Figure 2.6. As can be seen from this figure the thermal cycle during welding will dissociate the small high-density β'' precipitates, which is present in the artificial aged parent material, in the region close to the weld. Further away from the weld these precipitates will be coarsened and β' precipitates will grow at the expense of the β'' particles. The region close to the weld, where almost no hardening precipitates are present is often referred to as a fully reverted microstructure. This region will experience a dramatic loss in strength, but because of natural ageing, some of the strength will be recovered. As a result, the position of minimum strength is shifted to the partially reverted region where coarsening of the precipitates has taken place. This is illustrated in Figure 2.8. Studies have shown that the loss in strength at the position of minimum hardness can be as much of 50 % of the strength of the parent material[2].

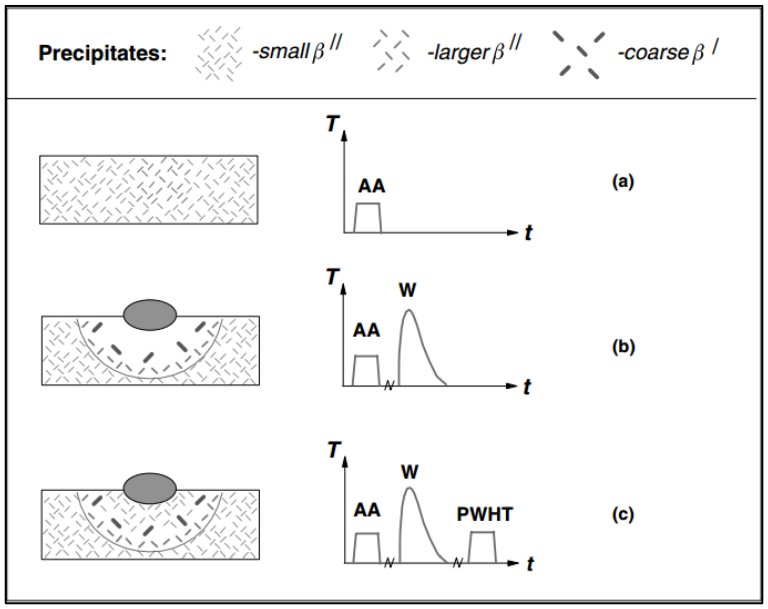

Figure 2.6: Microstructure evolution during thermal processing of AlMgSi-alloys. AA: artificial ageing, W: welding, PWHT: post weld heat treatment[11].

After welding, post weld heat treatment (PWHT) may be done to re-precipitate the hardening β'' precipitates close to the weld. This can recover some of the strength, but will not be sufficient to reach the strength in the parent material.

O. R. Myhr showed that the hardness profile can be modelled using two equations as showed in Figure 2.7. Equation 18 and 32, in the figure, refers to Equation 2.4 and Equation 2.5, respectively. Explanations of these equations can be found in Myhrs doctoral thesis[21].

Equation 2.4: Strength reduction in HAZ as a consequence of precipitate growth [21].

$$I_1 = X_d^{1/n_1} = (1-\alpha_1)^{1/n_1} = \int_0^t \frac{dt}{t_1^*}$$

Equation 2.5: Strength reduction in HAZ as a consequence of precipitate dissolution [21].

$$\alpha_3 = 0.56 X_{ss}^2 = 0.56\left[\left(\frac{\alpha_2}{0.56}\right)^{1/2} - \alpha_1\right]^2$$

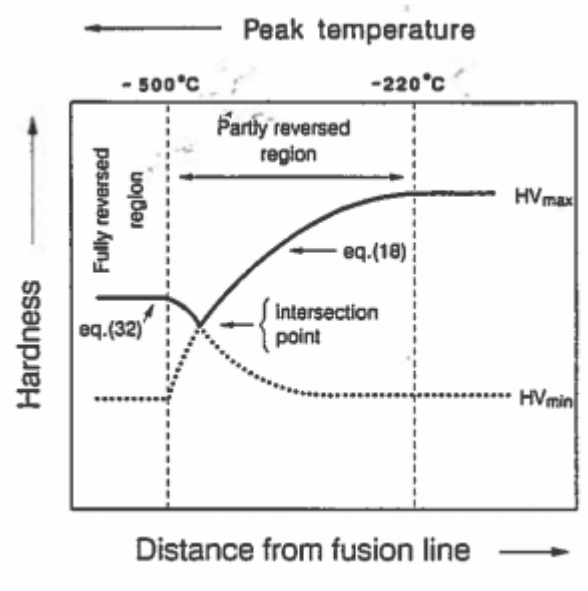

Figure 2.7: Modelling of hardness profiles as studied by O. R. Myhr[21]

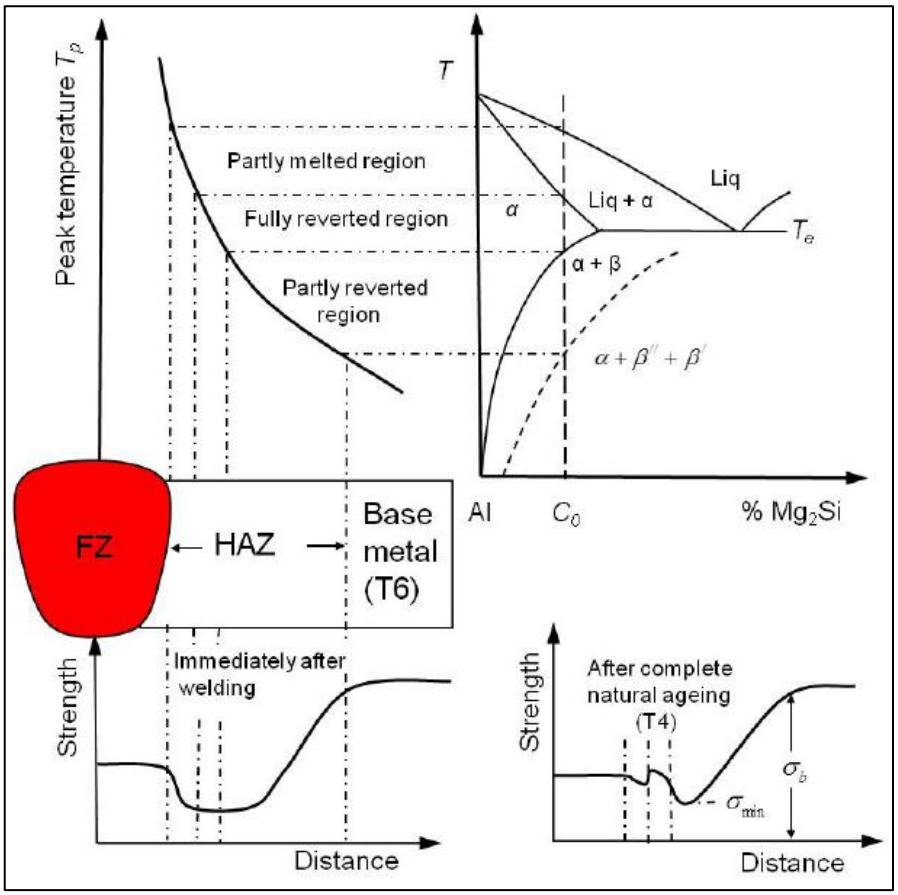

Figure 2.8: Microstructure and strength evolution during fusion welding. Top: Formation of various microstructural regions after single pass butt welding of a T6 tempered alloy. Bottom: Strength evolution through the HAZ of the profile immediately after welding and after complete naturally ageing[14].

2.5 Corrosion of aluminium

Although AlMgSi-alloys generally show excellent corrosion resistance, local corrosion types like intergranular corrosion (IGC) and pitting corrosion have been reported in numerous studies and for many alloys[6, 17, 20, 22-40]. These problems particularly arise for alloys containing copper and alloys with a Si-content in excess of what is needed to for Mg_2Si particles. In the following two sections, IGC and pitting corrosion will be reviewed in further detail. Further on, in section 2.5.3, corrosion in seawater and in section 2.5.4 corrosion of welded aluminium will be discussed.

2.5.1 Intergranular corrosion (IGC)

Intergranular corrosion is a type of localized corrosion that propagates along the grain boundaries of the metal. These attacks leads to a very characteristic look in the optical microscope, but is often very hard to spot with the naked eye. Although IGC often do not account for a large weight loss it can lead to serious reduction in mechanical properties and result in corrosion related cracks and ruptures[41].

IGC arises as a consequence of micro-galvanic coupling of either nobler or less noble particles on the grain boundaries and the surrounding region. The difference in potential between the grain boundary particles and the bulk is caused by the small solubility of intermetallic phases in the aluminium matrix. For AlMgSi-alloys intermetallic phases containing Cu and/or Si are cathodic (ennobling) and Mg is anodic. The precipitation of these intermetallic phases on the grain boundaries also leaves a depleted region around the grain boundaries, often called the particle free zone (PFZ), which becomes active during intergranular corrosion. A conceptual sketch of the IGC mechanism for AlMgSi-alloys containing Cu is shown in Figure 2.9.

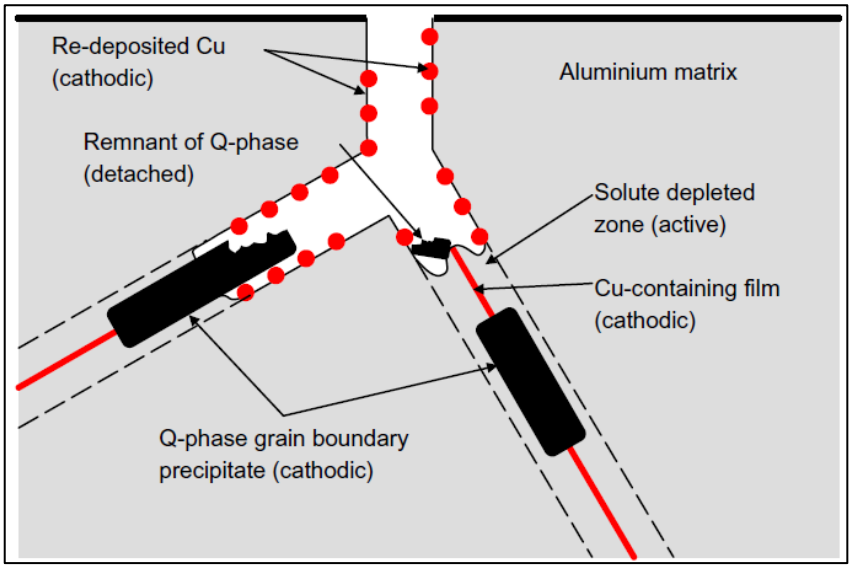

Figure 2.9: Conceptual sketch of IGC mechanism with Q-phase acting cathodic and the depleted region anodic[26].

There are many factors influencing IGC, but the main ones can be summarized as followed:

1. Chemical content[17, 22-27, 30, 32, 33, 37]
2. Heat treatment [17, 24-26, 30, 33, 34]
3. Microstructure [28]

In the following, the effect of main alloying elements, artificial ageing, cooling rate after extrusion and microstructure on IGC in AlMgSi-alloys will be discussed.

Effect of Cu

Copper is used extensively in aluminium alloys to increase strength, but has a negative effect on corrosion resistance, especially resistance to intergranular corrosion. In fact, copper is said to be the most dominating element contributing to IGC[33, 37]. This is a result of precipitation of a continuous copper rich phase along the grain boundaries[17, 23, 26, 30, 33]. This phase is called the Q-phase and has a proposed chemical composition of $Al_4Mg_8Si_7Cu_2$, as descirbed in section 2.3. The Q-phase will act cathodic and activate the surrounding PFZ as shown in Figure 2.9. Although no lower limit to copper content with respect to IGC has been found, it has been showed that alloys with a copper content as low as 0.12 wt% is susceptible to IGC [30]. Recent studies has also shown that an addition of just 0.09 wt% Cu will increase the IGC dramatically[42].

Effect of Si and Mg

The addition of an Si-content in excess of what is required to form Mg_2Si-particles, i.e. Mg/Si<1.73 in wt%, has been reported to contribute to IGC[17, 22, 23, 32], but it has also been showed that it has a rather small significance compared to Cu[33]. The corrosion mechanism is showed in Figure 2.10. It is believed to start at the Mg_2Si-particles and thereby propagate to the PFZ surrounding the particles at a later stage. Si also plays a vital role in establishing active zones at the grain boundaries, which is necessary in order to stimulate the propagation of IGC[25].

Mg in solid solution is not believed to contribute to corrosion as the change in corrosion potential is reported to be minimal[38]. Mg can however combine with Al and form anodic phases which can contribute to IGC. This may be an issue during welding as Mg rich filler metals often are used.

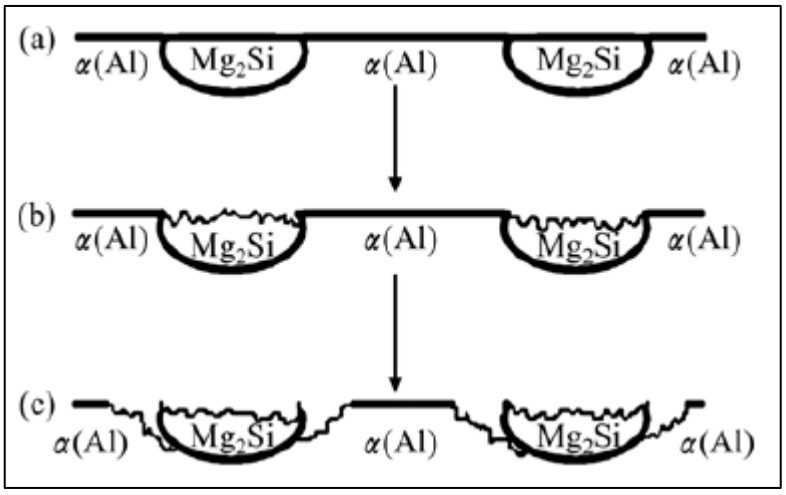

Figure 2.10: Conceptual sketch of corrosion mechanism of Mg_2Si precipitates. (a) Mg_2Si particles at grain boundary, (b) corrosion starts at Mg_2Si particles, (c) corrosion of PFZ at later stage[32].

Effect of Mn and Fe

Fe in small additions is not regarded as a problem concerning IGC, it can however influence the pitting corrosion behaviour by forming phases with aluminium (Al_3Fe and Al_6Fe). These phases may cause severe attacks in the form of pitting corrosion in aluminium alloys [22, 43, 44]. This can be counter effected by the addition of Mn, as it will combine with Fe and form less harmful AlMnFe-particles[43]. These phases may also combine with Si, and thereby improving the resistance to IGC. Another beneficial property of Mn is that it can restrict grain boundary precipitation and thereby reduce IGC[16].

Effect of Zn

Zn has the effect of shifting the corrosion protection in a more negative direction. This should thereby oppose the effects of Cu. However, the additions of up to 0.5 wt% Zn has not shown any beneficial effect on the overall corrosion behaviour[16].

Effect of artificial ageing

Artificial ageing to a temper of peak strength (T6) is traditionally believed to increase the susceptibility to IGC. This effect was first reported by Mondolfo in 1976[16] and later confirmed by El-Menshavy et al.[34]. Recent studies, on the other hand, have shown a decrease in IGC susceptibility in the T6 condition. This inconclusiveness between the different studies is probably related to the complex nature around and the many factors influencing IGC.

A suggested mechanism behind the changes in IGC susceptibility with ageing time proposed by Svenningsen et al.[26] is shown in Figure 2.11. For the underaged sample, the cathodic film on the grain boundaries is continuous and thereby leaving the material very susceptible to IGC. During ageing this cathodic film is coarsened and gets discontinuous, thereby reducing the driving force for

IGC. The overaged sample has coarse matrix precipitates giving pitting corrosion. In fact, all mentioned studies reported increased susceptibility for pitting corrosion with increased ageing time.

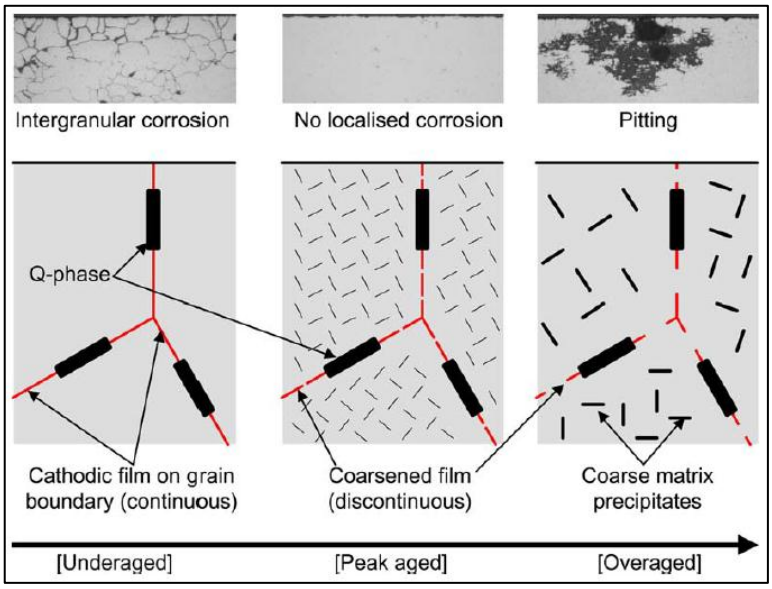

Figure 2.11: Suggested mechanism behind change in IGC susceptibility with artificial ageing time[26].

The effect of artificial ageing time on solution heat treated alloys is shown in Figure 2.12, as reported by Svenningsen et al.[26]. A clear tendency to less susceptibility to IGC with increasing ageing time is evident up to peak strength. In fact, the T6 sample showed no localized corrosion. For the overaged sample, however, clear signs of pitting corrosion was visible.

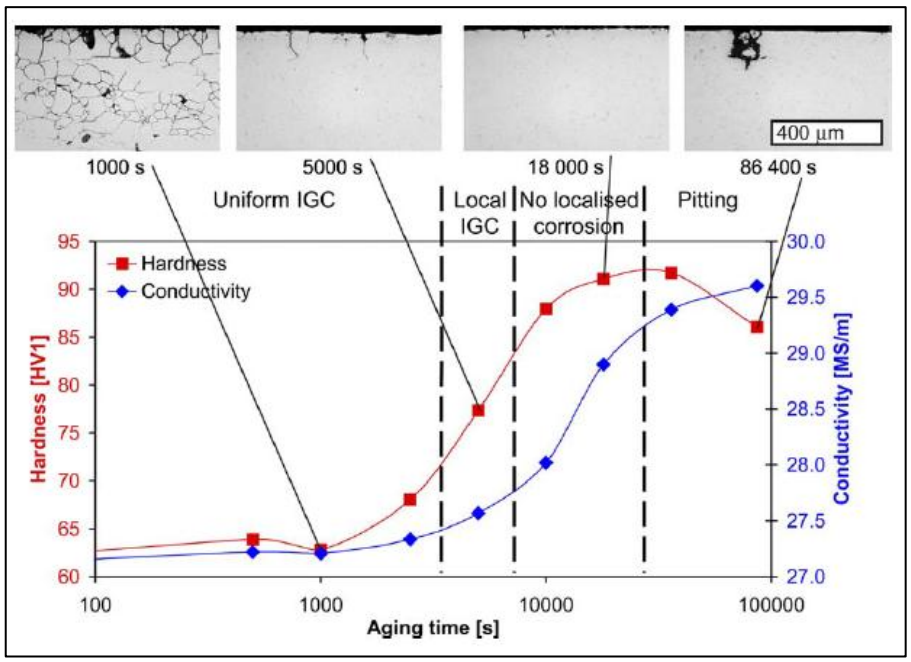

Figure 2.12: Results reported by Svenningsen et al.[26] on the effect of artificial ageing time with respect to localized corrosion.

Effect of cooling rate after extrusion

Recent studies by Svenningsen et al.[24-26] has showed that the cooling rate after extrusion can influence the IGC susceptibility. The studies showed that water quenched samples were less susceptible to IGC attacks than the air cooled ones. This is attributed to the precipitation of Q- and Mg_2Si-phases on the grain boundaries of the air cooled samples, whereas the water quenched sample had limited precipitation of these phases. The difference in the IGC attacks is depicted in Figure 2.13.

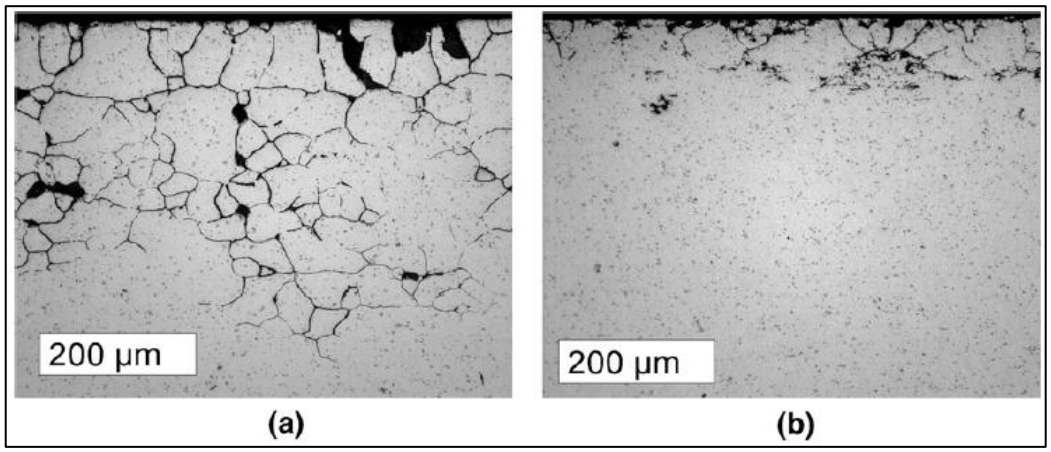

Figure 2.13:Micrographs of (a) air cooled and (b) water quenched sample after accelerated corrosion test[25].

Effect of microstructure

Studies suggests that there may be a correlation between the grain boundary angle and the susceptibility to IGC. This was shown that Minoda and Yoshida[28], who explained this correlation by stating that particle free zones (PFZ) and grain boundary precipitates form more easily on high angle boundaries as opposed to low angle boundaries. Larsen[22] also showed that profiles with a recrystallized layer, with high angle grain boundaries, and a fibrous bulk, with low angle grain boundaries, where characterized by IGC attacks limited to the recrystallized layer.

2.5.2 Pitting corrosion

Pitting corrosion is, together with IGC, the most serious corrosion mechanism related to AlMgSi-alloys. It is strongly related to a local breakdown of the passivating film and forms attacks with a narrow opening. The only condition that has to be met for pitting corrosion to arise in aluminium is a media such as water, seawater or moist air. This means that pitting can be a problem in almost all natural environments, as the pH can be close to neutral[41]. Pitting corrosion in aluminium alloys has been the subject of many studies, but its mechanism is still not fully understood[36]. It is, however, useful to divide the mechanism in two separate stages; initiation and propagation.

Initiation

Initiation starts with a local breakdown of the passivating film. The proposed mechanisms for this include penetration, adsorption and film breaking, as illustrated in Figure 2.14[36]. It is not determined which of these mechanisms that is the dominating one. It is however accepted that the presence of aggressive Cl^--ions play a crucial role. These ions will attack weak points in the passivating film and form $AlCl^{4-}$, leaving a high density of micro-cracks at the surface. From these cracks, just a minute fraction will lead to pitting corrosion. Why just a minute fraction will developed is also not fully understood, but is believed to be related to a critical factor showed in Equation 2.6, where *x* is pit depth and *i* is current density[45].

Equation 2.6: Critical factor for pit initiation.

$$critical\ factor: x \cdot i$$

The value of this factor can be used to determine the current density required to initiate or sustain pitting at a defect of a given size.

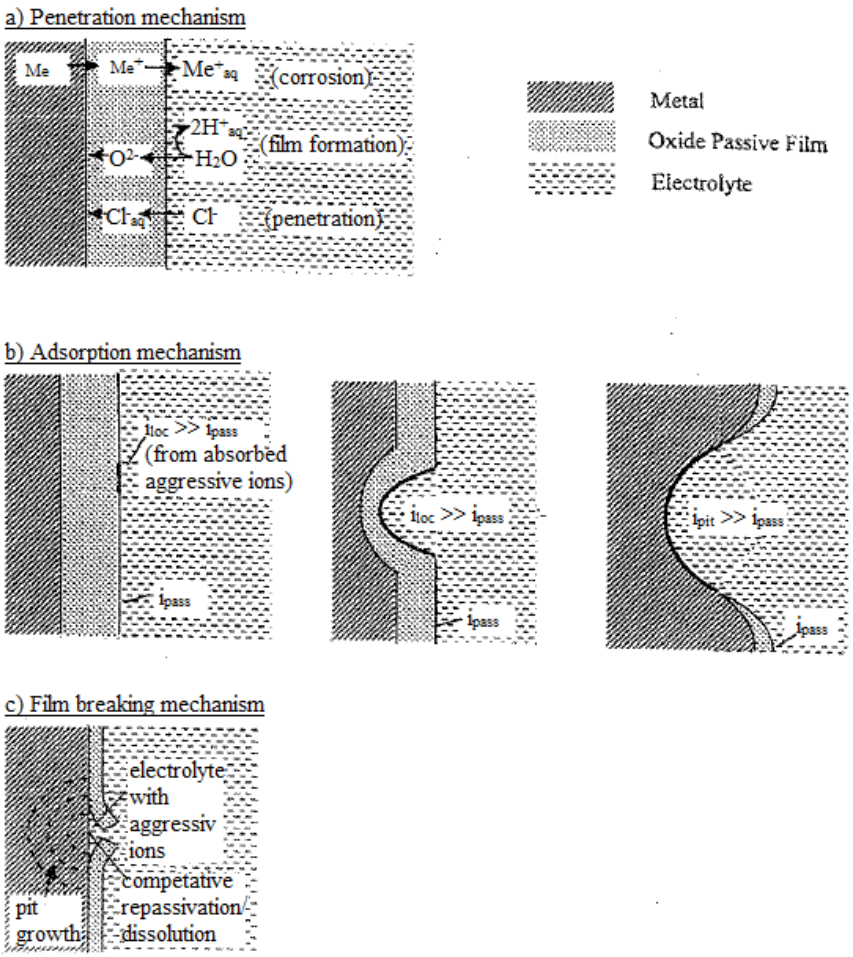

Figure 2.14: Three proposed initiation mechanisms as proposed by Frankel[36]. a) penetration, b) adsorption and c) film breaking. Me: metal[36].

Propagation

After a stable pit is formed the chloride ions will migrate to the bottom of the pit and dissolve Al as in Equation 2.7.

Equation 2.7: Anodic reaction at the bottom of the pit.

$$2Al \rightarrow 2Al^{3+} + 6e^{-}$$

The cathodic reactions takes place at intermetallic particles close to the pit and are hydrogen and oxygen reduction as shown in Equation 2.8.

Equation 2.8: Cathodic reactions at intermetallic particles a) hydrogen reduction and b) oxygen reduction.

$$a)\ 3H^{+} + 3e^{-} \rightarrow \frac{3}{2}H_2$$

$$b)\ \frac{3}{2}O_2 + 3H_2 + 6e^{-} \rightarrow 6OH^{-}$$

Because the cathodic reactions either use H^+ or produce OH^-, the pH will increase locally around these intermetallic particles and cause etching of the aluminium matrix surrounding these particles[46]. The overall reaction is showed in Equation 2.9 and leaves a white corrosion product, often visual to the naked eye. Hydrolysis of dissolved aluminium will also occur in the pit, causing the pH to be lowered, as showed in Equation 2.10.

Equation 2.9: Overall reaction for pitting corrosion in aluminium alloys.

$$2\mathrm{Al} + 3\mathrm{H_2O} + \frac{3}{2}\mathrm{O_2} \rightarrow 2\mathrm{Al(OH)_3}$$

Equation 2.10: Hydrolyses of dissolved aluminium ions in the pit.

$$Al^{3+} + 3H_2O \rightarrow Al(OH)_3 + 3H^{+}$$

As the cathodic reactions take place at intermetallic particles, as showed in Figure 2.15, these are of upmost importance when dealing with pitting corrosion.

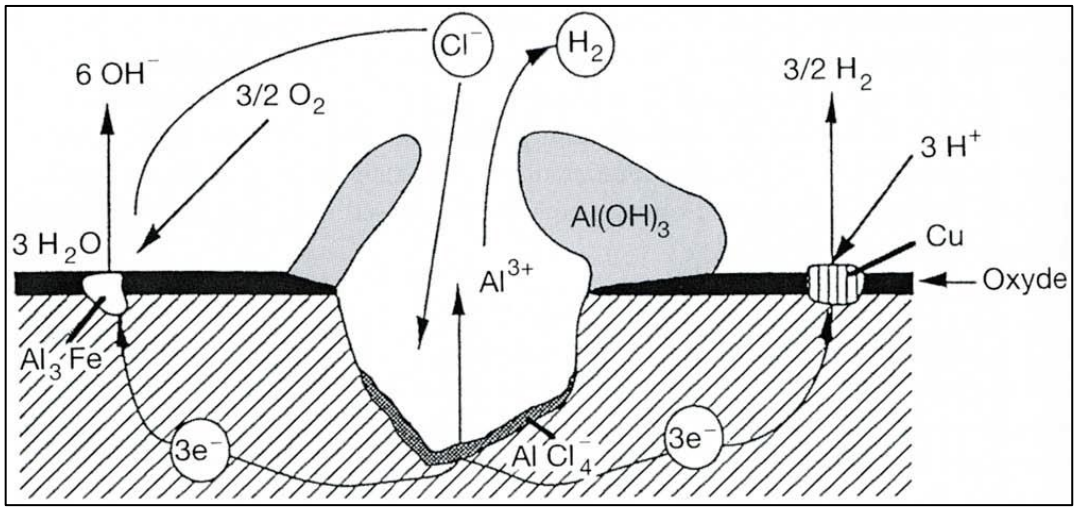

Figure 2.15: Suggested mechanism for pitting corrosion of aluminium alloys[41].

Effect of alloying elements

Intermetallic particles form because of low solubility of most alloying elements in aluminium alloys, either during casting (primary particles/dispersoids), homogenization (dispersoids) or artificial ageing (precipitates). The main particles that form in AlMgSi-alloys are considered to be Fe intermetallics and Mg_2Si precipitates[47].

K. Nisancioglu[43] studied the effect of Fe, Mn and Si on intermetallic phases in NaOH solutions. It was showed that Al_3Fe phases were dealloyed of Al when subjected to the solution. Depletion of Al from the particles was found to be detrimental to the cathodic behaviour, due to the formation of a Fe-rich protective oxide on the surface of the particle. This effect was, however, counteracted by enrichment on the surface of the particle of Si or Mn, leading to a reduction of both the cathodic and anodic reaction rate.

The effect of Mg and Si is still not clear. Studies by Eckermann et al.[47] showed that the selective dissolution of Mg on MgSi phases started immediately after immersion of the samples in a 1 M NaCl solution. Because of this, Si-oxides are left in the matrix which are insulating and does not contribute to corrosion. However, if other intermetallic particles are inactive, MgSi phases can cause corrosion by increasing the cathodic current density.

Cu seems to increase the pit density during the initiation stage. In fact, the pit density for AA1199 was found to increase from 100 pits per cm^2 to 1000 pits per cm^2 in an alloy containing 4 wt% Cu[48]. Cu located in solid solution is nobler than the aluminium matrix and the pitting potential is reported to increase significantly with increasing Cu content[29]. However, if Cu forms intermetallic phases, they can be either nobler or less noble than the aluminium matrix. Some phases commonly observed in aluminium alloys are presented in Figure 2.16, together with their dissolution potential.

Solid solution	Dissolution potential (mV SCE)	Intermetallic phase
	−170	Si
	−430	Al_3Ni
	−470	Al_3Fe
Al–4Cu	−610	
	−640	Al_2Cu
Al–1Mn	−650	
1050A	−750	
	−760	Al_6Mn
Al–3Mg	−780	
Al–5Mg	−790	
Al–1Zn	−850	
	−910	Al_2CuMg
	−960	$MgZn_2$
Al–5Zn	−970	
	−1150	Al_3Mg_2
	−1190	Mg_2Si

Figure 2.16: Dissolution potential of solid solution and some intermetallic phases commonly observed in aluminium alloys[49]

2.5.3 Corrosion in seawater

Nisancioglu[46] studied corrosion and corrosion protection of aluminium alloys in seawater and stated that *"pitting, flow-dependent corrosion and erosion corrosion are the basic corrosion problems for aluminum alloys in seawater"*. This is explained by noting that the uniform corrosion rate under stagnant flow-rate conditions lie below 1 µm/y and that crevice corrosion is normally not a problem. Erosion corrosion is caused by particles in a flowing media hitting the surface, breaking the protective layer and thereby exposing the base metal. This can be a serious problem for aluminium alloys and can increase the corrosion rate with many orders of magnitude. However, as erosion corrosion is mainly controlled by the speed and hardness of the particles, it can be considered as a design problem. The most effective protection against erosion corrosion is protective coating.

Effect of flow rate

In stagnant and low flow rates, localized corrosion in the form of pitting and IGC is the main issue. For higher flow rates, the chemical dissolution of the oxide layer will increase and uniform corrosion will thereby be the dominant corrosion issue. In Figure 2.17 the corrosion rate is shown as a function of flow velocity. The line is calculated by mass transfer considerations and shows the uniform corrosion rate.

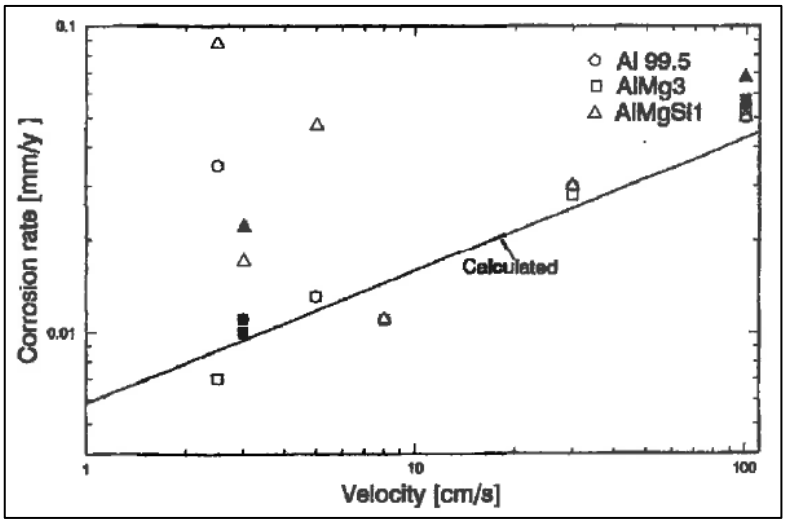

Figure 2.17: Flow velocity vs. corrosion rate as reported by K. Nisancioglu[46]. Open circuit conditions (open) and cathodic protection at -1.0 VSCE (bold).

Cathodic protection has proven to be very efficient at low flow rates. However, at higher flow rates cathodic protection may increase the corrosion rate, as can be seen in Figure 2.17.

Effect of temperature

It is generally acknowledged that an increase of the temperature will increase the corrosion rate of aluminium alloys[50]. In a recent study by H. Ezuber et al.[35] this effect was clearly demonstrated for AA1100 and AA5083. For an increase of the temperature from 23 to 60 °C, both the pitting and corrosion potential was lowered with about 200mV and the passive current density increased with about one order of magnitude. These findings are shown in Figure 2.18 and was explained by the increase of temperature *"facilitates oxygen diffusion to the alloy surface and, thereby, creating higher concentration of corrosion cells".* The change in pitting potential has also been reported to be related to changes in the hydration degree of the oxide film[40].

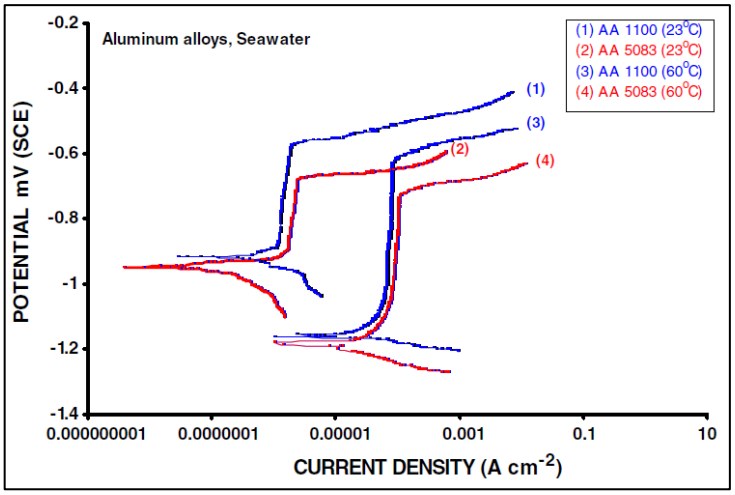

Figure 2.18: Effect of increased temperature on polarization curves as reported by H. Ezuber et al.[35]

In 1976, Van de Ven and Koelmans[51] reported that the cathodic corrosion of aluminium has two distinct temperatures regions. The high temperature region is independent of temperature, whereas the low temperature region is highly dependent on temperature. This was explained by the cathodic corrosion is limited by the dissolution of Al, which showed a very similar temperature dependency.

Not many studies concerning corrosion at low temperatures, such as temperatures in the arctic region, have been published. Based on the mentioned studies it may be expected that the corrosion rate, and especially the cathodic corrosion, will decrease.

Effect of exposure time

In the case of erosion and flow-dependent corrosion the relation to exposure time will be of a linear type, because these corrosion types are related to a global degradation of the passivating film. For pitting corrosion Bardal[52] studied the effect of exposure time for the depths of pits in AlMgSi-alloys when exposed to artificial sea water. The findings are shown in Figure 2.19, and it was found that the depth of pits could be described by the relation showed in Equation 2.11.

Equation 2.11: Relationship between depth of pits and exposure time[52].

$$d = Kt^{1/3}$$

Where d is pit depth in micrometers, t is the time of exposure in months and K is a constant dependent on type of alloy, exposed area and environment. Although this relationship may seem straight forward, it is not always valid and the exponent may deviate substantially from 1/3, especially during the initiation stage.

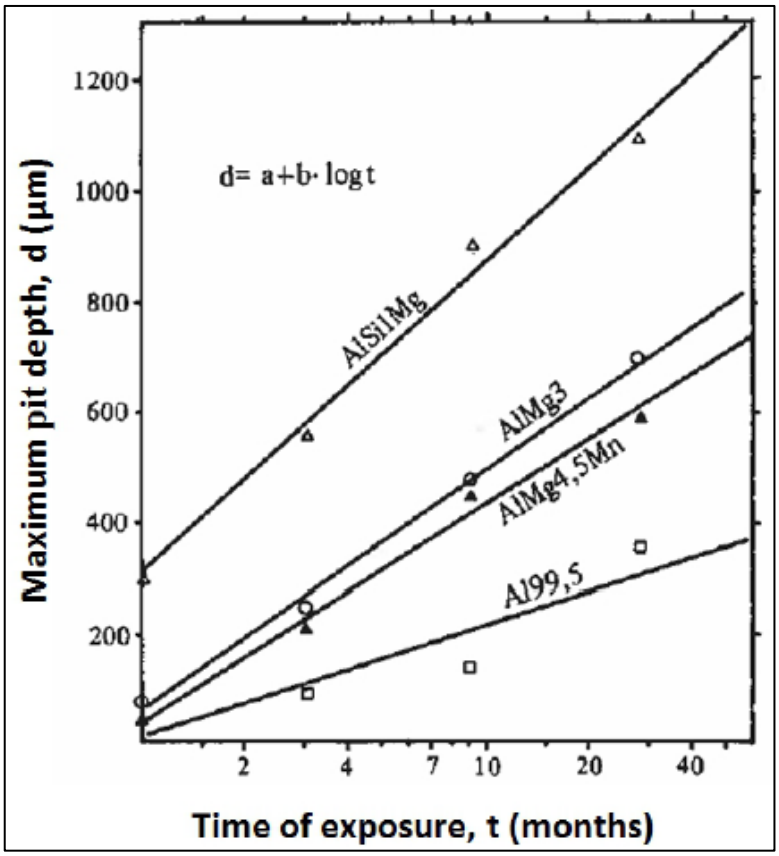

Figure 2.19: Maximum depth of pits vs time of exposure for some AlMgSi-alloys[52]

Environmental factors

Although the environmental factors in the sea will be dependent on geography, especially temperature and salinity, some general observations can be done. In Figure 2.20, the temperature, oxygen content, pH and salinity in seawater is shown as a function of depth as found by Vargel[53]. The salinity increases with increasing depth. This is because the density will increase with increased salinity. Temperature decreases with increasing depth and reaches a minimum of about 2 °C. Oxygen contents and pH have a similar development as a function of depth, this is because they are dependent on microorganisms and photosynthesis. A comprehensive study of these factors is not within the scope of this study, but from the figure it can be seen that they both reach a minimum at around 600 m below the surface. It should be mentioned however that the high oxygen content at the surface is caused by the enrichment of oxygen from the air as waves will mix the air and the water.

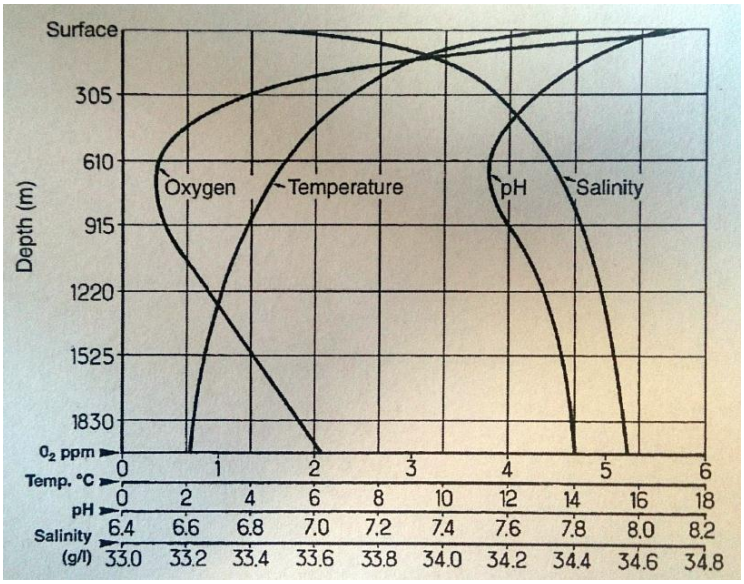

Figure 2.20: Oxygen content, temperature, pH and salinity in seawater as a function of depth.

In Figure 2.21, measurements of salinity and temperature from the most northern metering station in Norway, located at Ingøy, is presented. The salinity follows the same development as for the previous figure, but the temperature does not. This is due to the very small variations in temperature as a function of depth in this region.

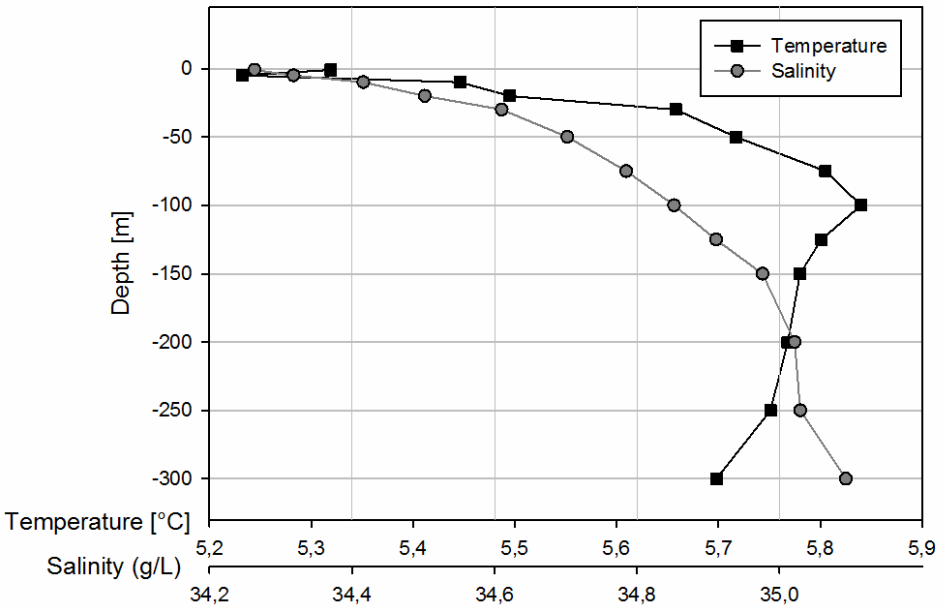

Figure 2.21: Temperature and salinity as measured at the metering station at Ingøy by the Instituite of Marine Research[54]

2.5.4 Corrosion of welded aluminium alloys

Corrosion of welded aluminium alloys has got more attention during the last decades, especially corrosion of friction stir welded (FSW) alloys. The rising interest is mainly driven by the lack of detailed and comprehensive studies available on the subject[55]. Some studies do exist however and in the following paragraphs the studies with relevance to this study will be presented.

Y. Ruan et al.[56] studied the corrosion behaviour of automatic MIG-welded AA6082-T6 with filler wire ER5356 containing 4.88 wt% magnesium. The study revealed pitting corrosion on both the base material and weld seam. Uniform corrosion and some IGC were also found on the weld seam, but not on the base material. The authors concluded that the base material displayed improved corrosion resistance compared to the weld seam.

Fahimpour et al.[57] did a comparison study of gas tungsten arc welding (GTAW) and FSW with respect to corrosion behaviour of a AA6061 in T6 condition. For the GTAW samples a filler wire containing 5 wt% Si was used (AA4043). The authors discovered that the most aggressive corrosion attacks took place in the welded section and that FSW provided improved corrosion resistance compared to GTAW. Moreover, post weld heat treatment (PWHT) was found to improve the corrosion resistance and in some cases the PWHT sample showed better corrosion resistance than the base material.

Maggioloni and Schmid[58] also did a comparison study between GTAW (tungsten inert gas (TIG)) and FSW with respect to corrosion of AA6082 and AA6060 in T6 condition. This study also found a reduced corrosion resistance in the welded region compared to the base material and that FSW provided better corrosion resistance than GTAW. The polarization curves from this study, shown in Figure 2.22, illustrate these findings by the lowering of the corrosion potential for the welded samples.

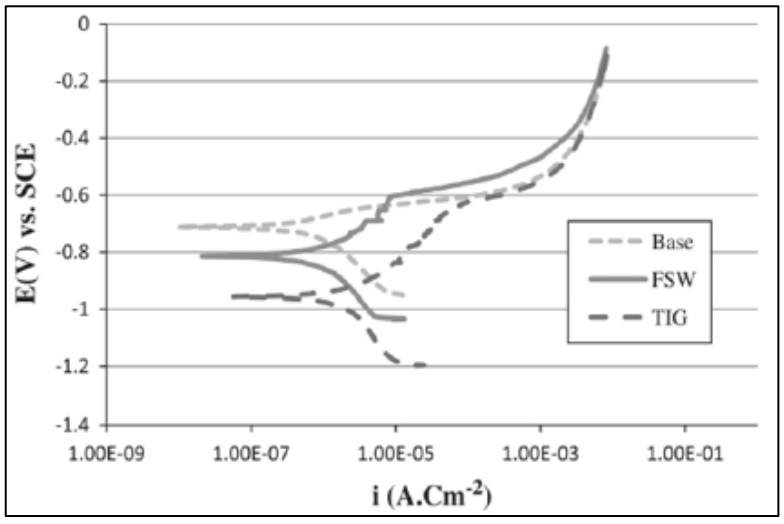

Figure 2.22: Polarization curves for base material and samples welded by GTAW (TIG) and FSW[58].

In Figure 2.23, the polarization curves after PWHT is shown. As the curves are shifted in a less negative direction, the corrosion resistance was improved after this treatment and the difference in corrosion resistance between base material and welded samples was eliminated.

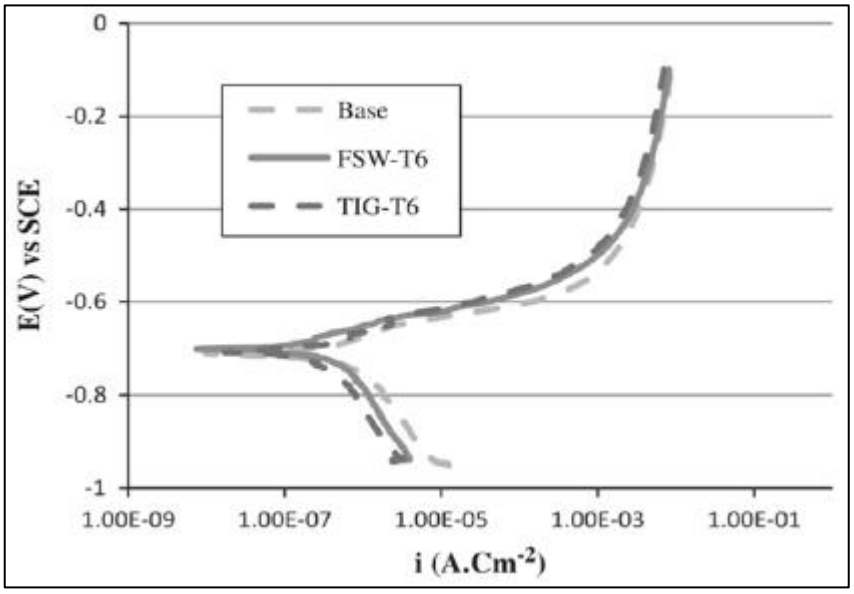

Figure 2.23: Polarization curves for base material and samples welded by GTAW and FSW after post weld heat treatment[58].

Metwally and Mosalam[20] studied the effect of filler wire on corrosion resistance for aluminium alloys. Two Mg-rich filler wires (AA5356 and AA5183) and one Si-rich filler wire (AA4043) was investigated and it was found that the Mg rich filler wires were more susceptible to IGC than the Si-rich filler wire. This was explained by the formation of active Mg_2Al_3 phases along the grain boundaries.

K.Srinivasa Rao and K.Prasad Rao[55] did a review of pitting corrosion of heat-treatable aluminium alloys and welds and found that the corrosion potential of the weld could be both higher and lower than the base material. This is due to the many different alloys and filler wires that can be used during welding. Another important aspect to consider is that if the weld metal is anodic compared to the base metal, the weld will protect the base by a cathodic protection. This can be very detrimental as the weld will have a much smaller area than the base material. It is therefore of upmost importance to choose the welding method and filler wire giving the best compromise between strength, cost and corrosion protection.

3 Materials and experimental procedure

3.1 Alloys

In this study, six different welded profiles of AA6082 with four different thicknesses were studied. To assess the corrosion properties of the different profiles they were subjected to an accelerated IGC-test, open circuit potential measurements and potential curve recordings at varying temperatures in artificial seawater. The chemical composition of the different profiles can be seen in Table 3.1, together with the specifications for the alloy. As can be seen from the table the profiles had a very similar composition and are well within the specifications for the given alloy.

Table 3.1: Chemical compositions, together with the specifications for ENAW-6082 according to EN 573-3[59]

	ENAW-6082	**10 mm**	**16 mm**	**20 mm**	**30 mm**
Si	0.7 – 1.3	0.93	0.99	0.99	0.97
Fe	Max 0.50	0.18	0.18	0.17	0.16
Cu	Max 0.10	0.008	0.025	0.025	0.004
Mn	0.40 – 1.0	0.55	0.56	0.56	0.54
Mg	0.6 – 1.2	0.60	0.64	0.63	0.63
Cr	Max 0.25	0.011	0.011	0.011	0.013
Zn	Max 0.20	0.002	0.005	0.006	0.004
Ti	Max 0.10	0.011	0.022	0.018	0.013

All profiles were welded by hand (hereon denoted by H). In addition, the 10 mm and 30 mm profiles were welded semi-automatically (hereon denoted 10A and 30A). The different material characterizations and corrosion tests performed on the different profiles are summarized in Table 3.2.

Table 3.2: Overview over characterization and corrosion tests performed.

	10A	10H	16H	20H	30A	30H
Macro etch	X	X	X	X	X	X
Optical microscope	X	X	X	X	X	X
Hardness curves	X	X	X	X	X	X
Particle analysis		X	X	X		X
Electrical conductivity	X	X	X	X	X	X
IGC	X	X	X	X	X	X
Open circuit potential					X	
Polarization curves	X					
Weld simulation		X				

3.2 Process route

In the following, the process route of the extruded flat bars will be presented. This includes casting, homogenization, extrusion, artificial ageing and welding.

3.2.1 Casting and homogenization

Casting of the billets was performed at Hydro Karmøy by direct chill (DC) casting. After casting, homogenization was done at 580 °C with a holding time of 3 hours. During homogenization the heating rate was 100 °C/h and cooling rate was 300-350 °C/h.

3.2.2 Extrusion and artificial ageing

The billets were extruded into flat bars at Hydal Aluminium Profiler at Raufoss, Norway. The extrusion parameters were not accessible from Hydro, but the dimensions of the flat bars were:

- 10 mm x 200 mm
- 16 mm x 160 mm
- 20 mm x 200 mm
- 30 mm x 200 mm

Artificial ageing was performed at 175 °C with a holding time of 5 hours and 30 minutes for the 10 mm flat bar and at 185 °C with a holding time of 5 hours and 10 minutes for the others.

3.2.3 Welding

Welding was performed by a certified welder at Marine Aluminium A.S. and standard welding procedures used under normal production at Marine Aluminium was used. The welder qualification and the welding procedure specification (WPS) are in accordance with EN 1090-3[60]. The

temperature of the HAZ was checked to be below 100 °C before the next layer of welding was performed. The weld consumable used, i.e. filler wire, was Safra 5183 with 4.3-5.2 wt% Mg and 0.5-1-0 wt% Mn. The shielding gas was Argon 4.0.

The numbering of the weld layers can be seen in Figure 3.1, together with the placement of thermocouples during welding. The welding parameters can be found in Appendix A.

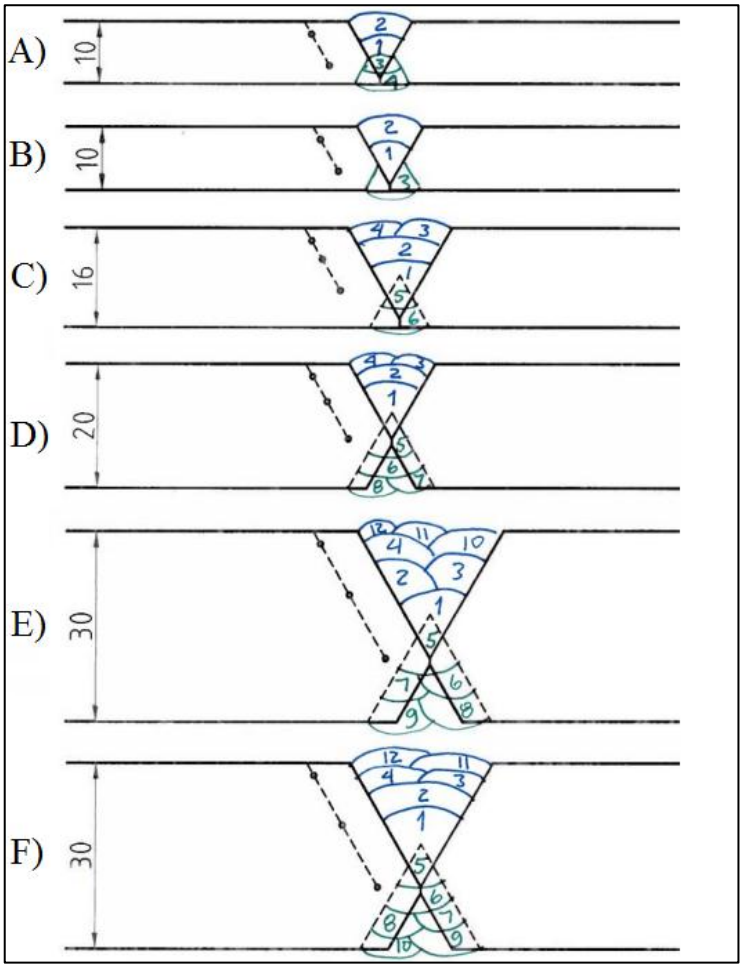

Figure 3.1: Numbering of layers and placement of thermocouples during welding. A) 10A, B) 10H, C) 16H, D) 20H, E) 30A, F) 30H

3.3 Material characterization

Before corrosion testing, material characterization of the samples was performed. This included macro etching, optical microscopy, hardness measurements, particle analysis in scanning electron microscope (SEM) and electrical conductivity measurements. In the following, the procedures of these examinations is described.

3.3.1 Macro etching

Macro etching of the cross section of all welds was performed following the *"Standard Test Method for Macroetching Metals and Alloys"*[61] table 1, top row. This included immersing the samples for 12 minutes in 10g NaOH /100mL H_2O, rinsing in water, immersing in strong HNO_3 and finally rinsing in water again.

3.3.2 Optical microscope

To review the grain structure of the material, optical microscope was used. Sample preparations were done in a series of steps starting with cutting and mounting in a ClaroCit resin. Then grinding was done by using successively finer grinding paper at P80, P320, P500, P800, P1200 and P2000 by use of a sample holder and a Stuers RotoPol31 with RotoForce-4 modular rotating preparation system. During grinding water was used as a lubricant. After grinding, polishing was performed by the use of 6 µm and 3 µm MD Mol and 1 µm MD Nap polishing discs. A Struers TegraPol31 with TegraForce-5 modular rotating preparation system was used for polishing. In between each polishing step the samples were rinsed in water and ethanol.

After polishing the samples were anodized in 5 % HBF_4 and 95 % H_2O with a current of 1 A and a voltage of 20 V for 90 seconds. Finally, the samples were rinsed in water and ethanol, and the air dried.

The optical microscope used was a Leica MEF4M with Jenoptik Laser Optik System camera connected to a personal computer with ProgRes Capture v2.8.8 software installed. The anodized samples were imaged with polarized light and a sub-parallel lambda plate. For microscopy of the base material the examined plane was in parallel with the extrusion direction and for the weld cross section it was perpendicular to the extrusion direction. This is illustrated in Figure 3.2.

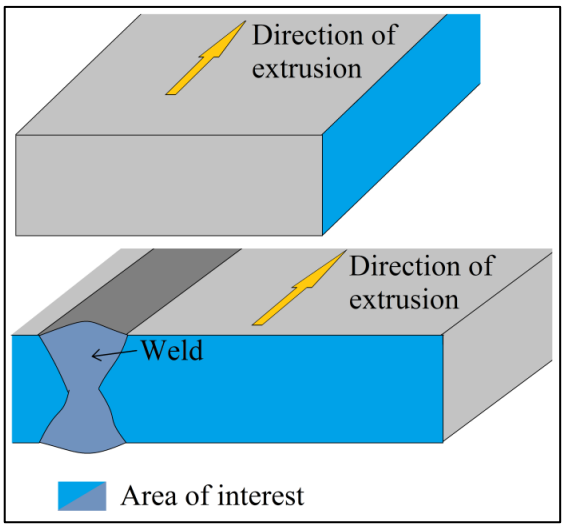

Figure 3.2: Area of interest during optical microscopy for base material (top) and weld cross section (bottom).

3.3.3 Hardness measurements

To investigate the effect on strength of welding, hardness of all samples through the welded region was measured. A Struers Duramin-A2500 hardness tester was used to find the Vickers hardness. All measurements were done with 1 kg load (HV1). The loading time for the measurements was 45 seconds. The measurements were done through the centerline of the profile with a distance between each measurement of about 1 mm. This is illustrated in Figure 3.3. The measurements were stopped when the hardness reached the known hardness of the base material.

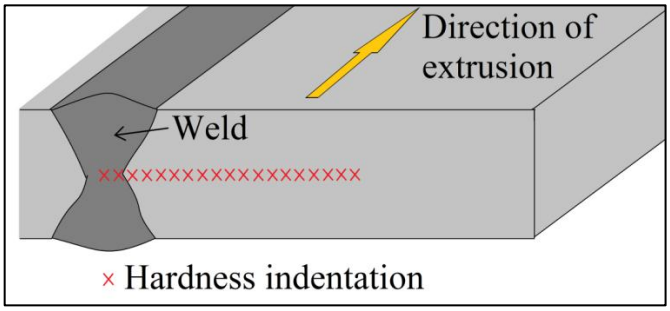

Figure 3.3: Position of hardness indentations with a distance of 1 mm between each measurement.

The cross section was cut using a Struers Discotom-5 with a 06TRE cut-off wheel. Before hardness measurements, the cross section was coarsely grinded with P80, P320, P500, P800 grinding paper in a successively finer order.

Hardness measurements of the base material were performed at the extrusion surface and no grinding were done.

3.3.4 Particle analysis

To characterize the primary particles and dispersoids, particle analysis was performed. This was done by using a Zeiss Supra VP Low Vacuum Field Emission Scanning Electron Microscope (LV-FESEM) with the main operating parameters as presented in Table 3.3. The sample preparation followed the same steps as for optical microscopy, except anodizing. Primary particles were photographed at 250x magnification and the dispersoids were photographed at 5000x magnification. All micrographs were taken in parallel with the direction of extrusion. To measure and analyze the particles, an unlicensed software *"ImageJ"* was used[62].

When using *"ImageJ"* the contrast and brightness of the recorded SEM-images was adjusted. Also a threshold of the particle count was set. This was done in the same fashion for all images, but some variation must be expected. To account for some of the variation, three images of each area of interest was analyzed. It should also be noted that this is not an analysis of the Mg_2Si-precipitates as such precipitates are too small to be correctly analyzed using SEM.

Table 3.3: Main parameters during particle analysis in LV-FESEM

Parameter	Value
Detector	Backscatter (AsB)
Acc. voltage	4.0 kV
Working distance	8.5 – 9.5 mm
Aperture radius	120 µm
Current	103 µA

3.3.5 Electrical conductivity

To measure the electrical conductivity in the base material, HAZ and weld seam a Foerster Sigmascope 2.069 was used. The instrument was calibrated before testing with calibrating samples that had a conductivity of 58.5 MS/m and 4.415 MS/m. A frequency of 920 kHz was used for all samples and the diameter of the probe was 7 mm. All measurements were done in the cross section of the sample. A total of three measurements for each position was performed.

3.4 Corrosion tests

3.4.1 Intergranular corrosion (IGC) test

To test for IGC susceptibility an accelerated corrosion test adapted from the British standard BS 11846 Method B[63] was used. This included cleaning the samples by rinsing in acetone and ethanol, followed by alkaline etching in a 70 g NaOH/L at 50-60 °C for 3-4 minutes. After etching, desmutting by immersing in a 65 % nitric acid (HNO_3) for one minute was done and then the samples were rinsed in distilled water.

The corrosion test itself consisted of immersing the samples in an aggressive corrosive aqueous solution containing 30 g/L NaCl and 10 mL/L 39 % HCl in 24 hours. All samples were separated during immersion to avoid intermetallic contact. After this they were once more immersed in nitric acid for one minute and rinsed in water. When rinsing, the samples were brushed with a plastic brush to remove any corrosion products.

Before testing, the samples were coated so that just the area of interest was left exposed to the solution. This, however, meant that weight measurements before and after exposure would not give a reliable result as the coating itself would be etched during exposure, and the degree of etching would depend on the amount of coating applied, which varied between the samples.

Visual inspection was done in the same way as for section 3.3.2, except these samples were not anodized during sample preparations. Number of attacks and depth of the deepest attack on the

inspected areas was recorded. The visual inspection was done perpendicular to the direction of extrusion.

3.4.2 Polarization curves

To assess the effect of temperature on corrosion behaviour in seawater, base material from the 10H sample were tested at 25 °C and 2 °C in artificial seawater. The preparations of artificial seawater followed ASTM D1141-98 method 7[64]. Before testing the samples were rinsed in acetone and ethanol, thereby an alkaline etch in 10 g NaOH/100 mL H_2O at 60-70 °C was performed, then immersing in 65 % HNO_3 for a couple of minutes and finally rinsing in water. This was done to ensure a clean and uniform surface, but at the same time keep the recrystallized layer intact. Two Julabo FT 200 "cold fingers" were used to lower the temperature for the samples tested at 2 °C.

A Gamry Potentiostat connected to a personal computer with Gamry Instruments Framework installed was used to record the polarization curves against a standard calomel reference electrode. The recordings started at 350 mV below and ended 300 mV above open circuit potential (OCP) with a sweeping rate of 0.5 mV/s. The working and counter electrode had a distance between them of 30 mm for all measurements. The samples were placed in a sample holder which provided an exposed area of 1.33 cm^2.

Gas bubbling of synthetic air and nitrogen gas was used to saturate and deplete the electrolyte for dissolved oxygen, respectively. Three parallels were performed for all parameters to confirm that the experiments were reproducible. A sketch of the experimental set-up is shown in Figure 3.4.

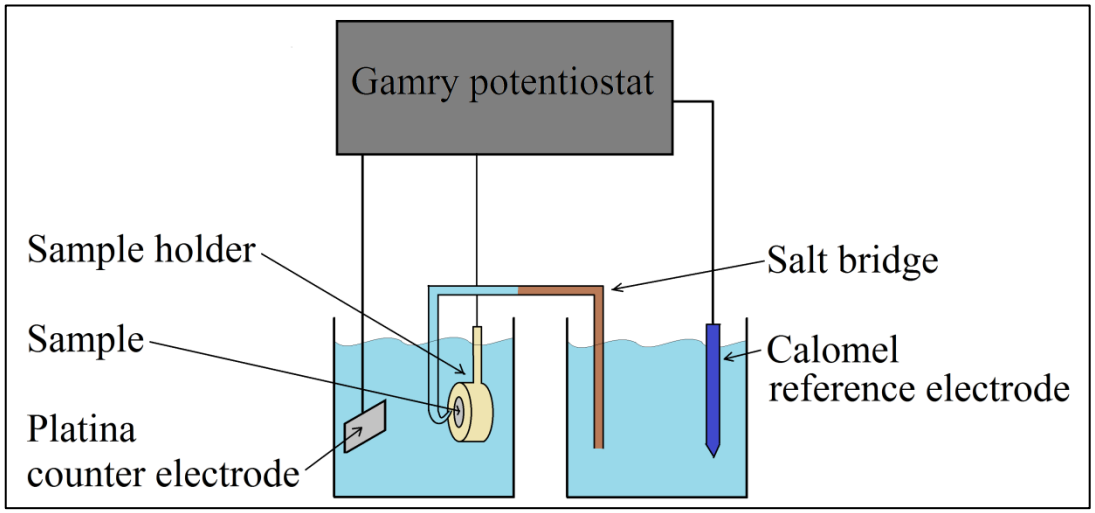

Figure 3.4: Sketch of experimental set-up for recording polarization curves and open circuit potentials.

3.4.3 Open circuit potential (OCP)

The same experimental set-up as for polarization curves was used for open circuit potentials (OCP). The samples were taken from the cross section of the base material from the 30 mm flat bar and

followed the same sample preparation as for the polarization curves. OCP was recorded over 12 hours with measurements made every 8th seconds. For OCP, only bubbling of synthetic air was used.

3.5 Weld simulations

To evaluate how to simulate multi-layer fusion welding and the impact of each layer on microstructure and strength distribution through the HAZ, weld simulations were performed. Such a simulation should ideally reflect the temperature profile and microstructural changes during fusion welding, except for the fusion zone itself as no melting of the material occurs during simulations.

Weld simulations were performed at Hydro R&D Center located at Sunndalsøra, using a Gleeble 3500 thermal system. The geometry of the samples, direction of extrusion and placement of thermocouple is illustrated in Figure 3.5. Base material from the 10 mm profile was used for all samples.

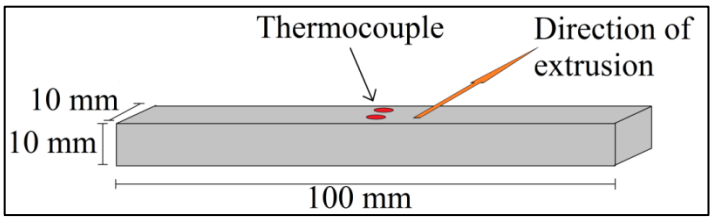

Figure 3.5: Geometry of samples and placement of thermocouple for weld simulations.

The samples were heated by direct resistance heating, which involves heating the samples by passing a direct current through two clamps at each side of the sample. The temperature evolution was monitored by a spot welded K-type thermocouple placed in the center line of the sample. The water cooled aluminium jaws at each side allowed efficient heat extraction. The experimental set-up for the weld simulations is illustrated in Figure 3.6.

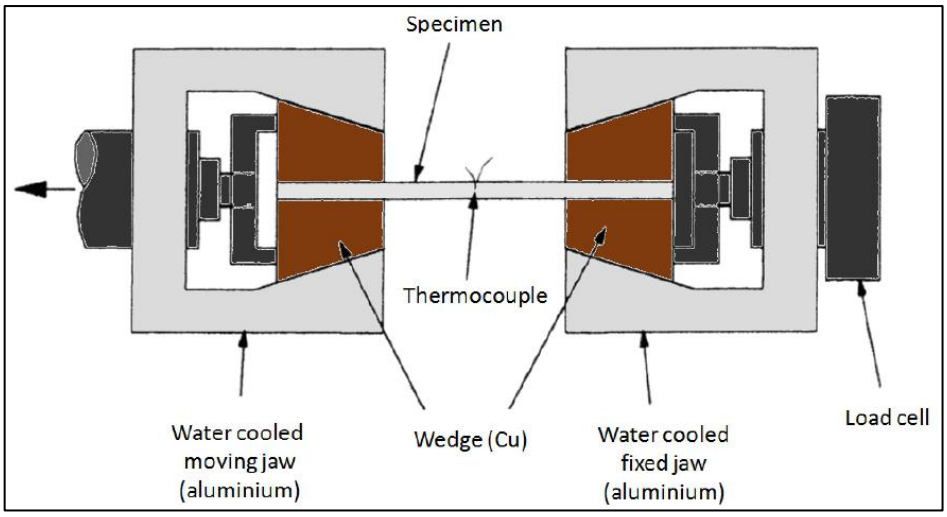

Figure 3.6: Experimental set-up for the Gleeble weld simulation station[65]. Figure not to scale.

3.5.1 Heat cycles

In order to simulate different positions in the HAZ, five different heat treatments were performed with either one or two heat cycles, in two parallels. The chosen heat cycles were a result of temperature recordings made during welding and adaptions made by Ole Runar Myhr at Hydro. The maximum temperature for each cycle is shown in Table 3.4. The 380-418 heat cycle is intended to simulate the strength at the position of minimum hardness. 340-360 intends to simulate a position further away from the weld than the position of minimum hardness and 530 is intended to simulate the fusion zone.

The recorded temperature curves for sample 380-418 (both parallels) are shown in Figure 3.7 and a complete collection of all temperature curves can be found in Appendix B.

Table 3.4: Maximum temperature and time at maximum temperature for all recorded temperature curves. Sample name indicate intended maximum temperature and parallel number in parenthesis.

	First heat cycle		Second heat cycle	
Sample	**Max temperature [°C]**	**Time [s]**	**Max temperature [°C]**	**Time [s]**
380-418 (1)	380.4	9.2	411.6	25.8
380-418 (2)	386.8	9.2	419.5	25.8
418-418 (1)	420.4	9.4	414.9	45.1
418-418 (2)	414.5	9.4	411.9	45.3
418 (1)	418.0	9.5	-	-
418 (2)	415.1	9.6	-	-
340-365 (1)	340.9	9.4	358.6	17.7
340-365 (2)	341.0	9.5	358.7	17.8
530 (1)	539.3	10.8	-	-
530 (1)	542.5	10.9	-	-

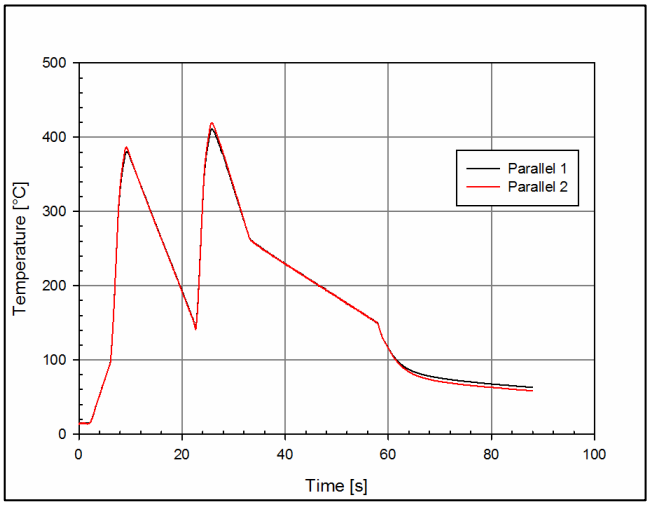

Figure 3.7: Temperature curves for the 380-418 samples during weld simulation.

3.5.2 Hardness curves

Hardness measurements of the weld simulated samples were performed in the same fashion as for the welded samples. The difference being that for the weld simulated samples, the measurements were done at both sides of the thermocouple and were performed in the extrusion surface, without any grinding prior to testing.

3.5.3 Tensile tests

Tensile tests of the weld simulated samples were performed at Institute for Material Science and Engineering at NTNU. The geometry of the specimens is shown in Figure 3.8. A MTS 810 hydraulic tensile testing machine with a maximum load of 100 kN was used to perform the tests, with an 25 mm extensometer. Both parallels of all heat treatments and two control samples, which had not been heat treated, were tested. The speed used was 2 mm/min.

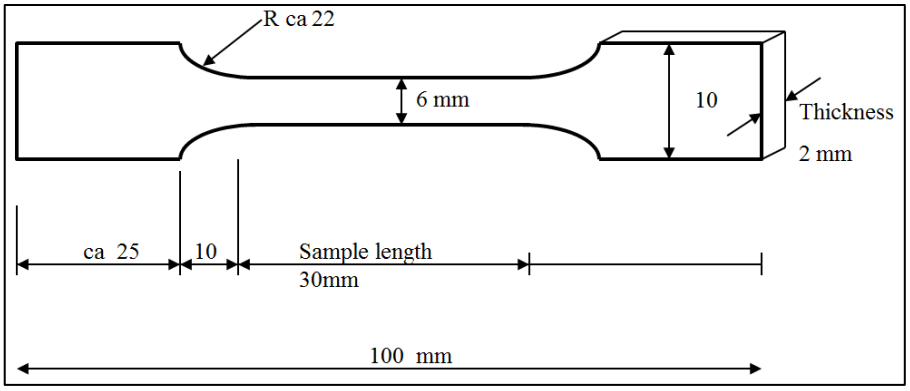

Figure 3.8: Specimen geometry for tensile tests of weld simulated samples.

4 Results

4.1 Material characterization

Prior to corrosion testing, material characterization of the received profiles was performed. This included macro etching, microstructure imaging of weld and base material, hardness testing, particle analysis and electrical conductivity measurements.

4.1.1 Macro etching

In Figure 4.1 macro images of the etched cross section of the weld for all samples are shown. The individual weld beads can be seen from these images, corresponding to the layering shown in Figure 3.1 in section 3.2.3. The heat affected zone (HAZ) cannot be seen by these images.

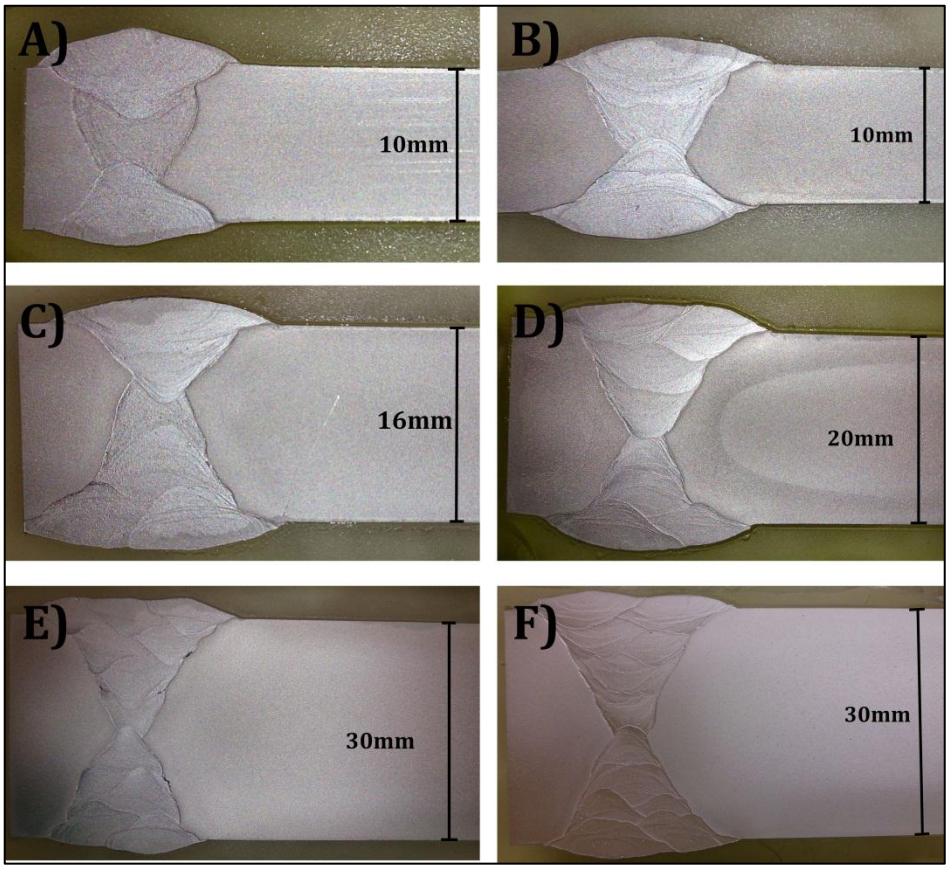

Figure 4.1: Macro image of etched cross section of weld for A) 10A, B) 10H, C) 16H, D) 20H, E) 30A, F) 30H

4.1.2 Microstructure

Optical micrographs of the base material are shown in Figure 4.2 through Figure 4.4 and in Figure 4.5 through Figure 4.7 the cross section of the weld is depicted.

Base material

Optical micrographs for 10A, 10H and 16H are shown in Figure 4.2. All display a typical microstructure for an extruded profile, with a fibrous microstructure in the center and a recrystallized layer towards the extrusion surface. The recrystallized layer for 10A and 10H is approximately 350 µm and for 16H the layer is approximately 330 µm.

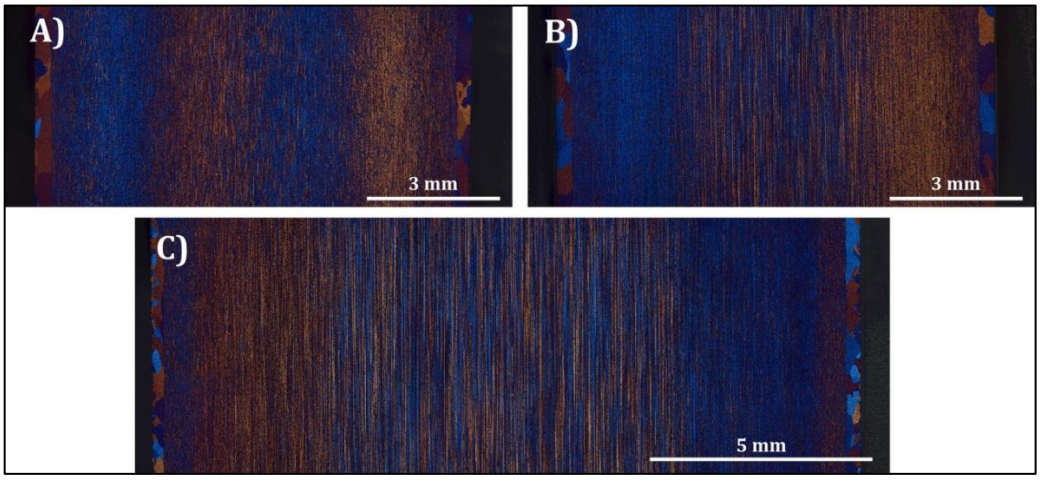

Figure 4.2: Optical micrographs of A) 10A, B) 10H and C) 16H. All displaying a typical microstructure for extruded profiles with a recrystallized layer of 360, 360 and 340 µm respectively. All micrographs are taken parallel with the direction of extrusion.

For 20H the recrystallized layer is considerably smaller, i.e. about 30 µm. This is shown in Figure 4.3, including a close up of the recrystallized layer. For 30A and 30H the recrystallized layer is barely visible and was measured to be less than 20 µm in the microscope. This is shown in Figure 4.4.

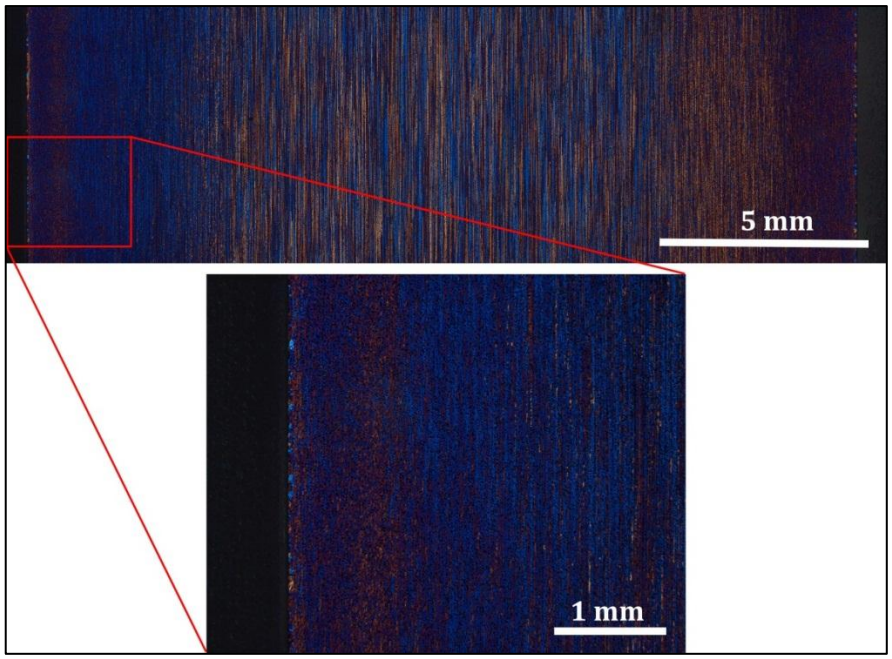

Figure 4.3: Optical micrograph of 20H, including a close up of the recrystallized layer. Micrographs are taken parallel with the direction of extrusion.

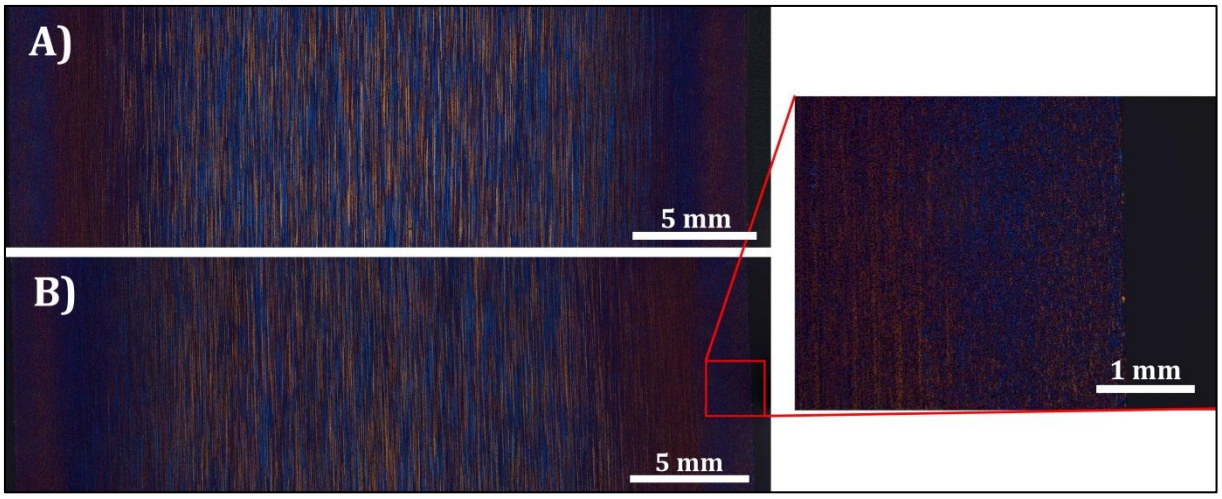

Figure 4.4: Optical micrographs of A) 30A and B) 30H, including a close up of the recrystallized layer. All micrographs are taken parallel with the direction of extrusion.

Weld

Micrograph of the complete cross section of the weld is showed in Figure 4.5 for 10A and 10H. The weld seams display an as-cast microstructure with equiaxed grains in the bulk of each individual weld bead and columnar growth between the weld beads and the fusion line and between the individual weld beads. Note also that the recrystallized layer seems to decrease in width towards the weld, especially for 10H.

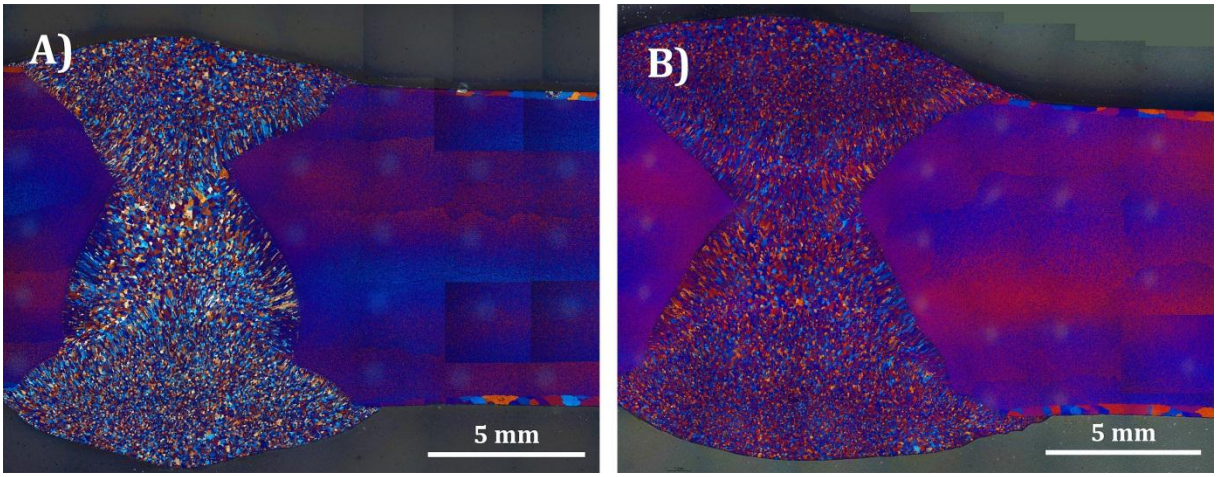

Figure 4.5: Weld cross section for A) 10A and B) 10H. Micrographs are taken perpendicular to the direction of extrusion.

In Figure 4.6 a selected area of the cross section of the weld of 16H is shown. This shows the same characteristics as 10A and 10H with as-cast microstructure in the weld seam with equiaxed and columnar growth. The same is also true for 20H, 30A and 30H, shown in Figure 4.7, but these profiles show no recrystallized layer close to the weld.

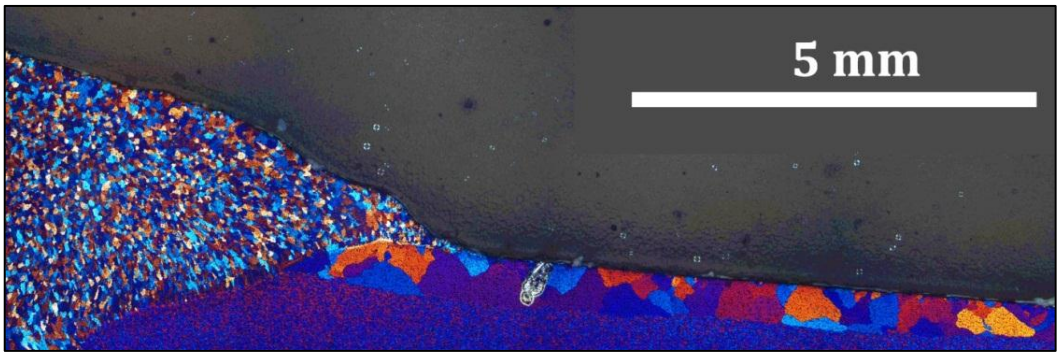

Figure 4.6: Micrograph of an selected area of the weld cross section of 16H. Taken perpendicular to the direction of extrusion.

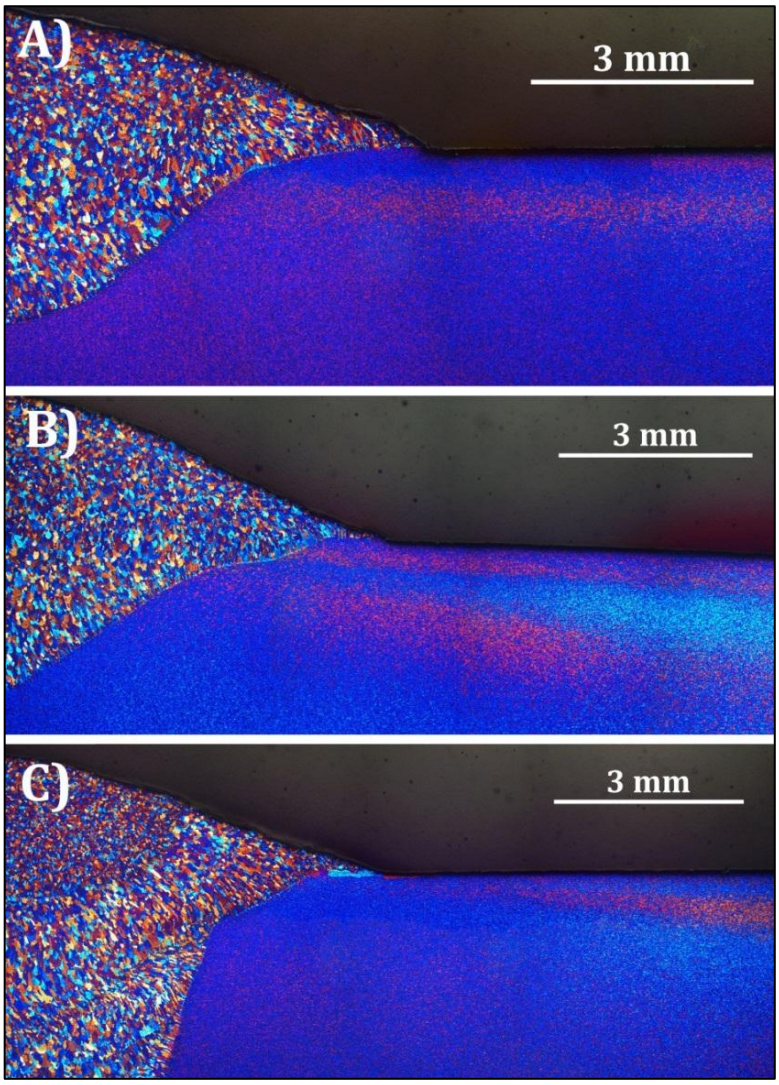

Figure 4.7: Micrograph of an selected area of the cross section of the weld for A) 20H, B) 30A, C) 30H. Taken perpendicular to the direction of extrusion.

4.1.3 Hardness profiles

Hardness values for the base material of all profiles considered in this study are presented in Table 4.1. As can be seen from the table, the hardness decrease as the thickness of the profile increases.

Table 4.1: Hardness of all profiles including standard deviation based on three indentations on the extrusion surface.

Sample	Hardness (HV1)	Standard deviation
10A	105	1,633
10H	105	1,414
16H	102	0,471
20H	97	2,055
30A	85	1,670
30H	85	0,816

Welded samples

Hardness profiles for all welded samples are presented in Figure 4.8 and Figure 4.9. Main results are also listed in Table 4.2

Table 4.2: Main results from hardness profiles of welded samples

Sample	Weld hardness [HV1]	Minimum hardness [HV1]
10A	74	61
10H	76	61
16H	85	65
20H	82	67
30A	89	60
30H	92	61

The hardness curves indicate that the position of minimum hardness is located about 7 mm from the weld center line for 10A, 10H and 16H. For 20H this position is 5 mm and for 30A and 30H it is about 6 mm from the weld center line. The base material hardness is reached at about 20 mm from weld center line for all samples. It should also be noted that the hardness of the weld bead seem to increase with increasing number of welding layers. All hardness measurements can be found in Appendix C.

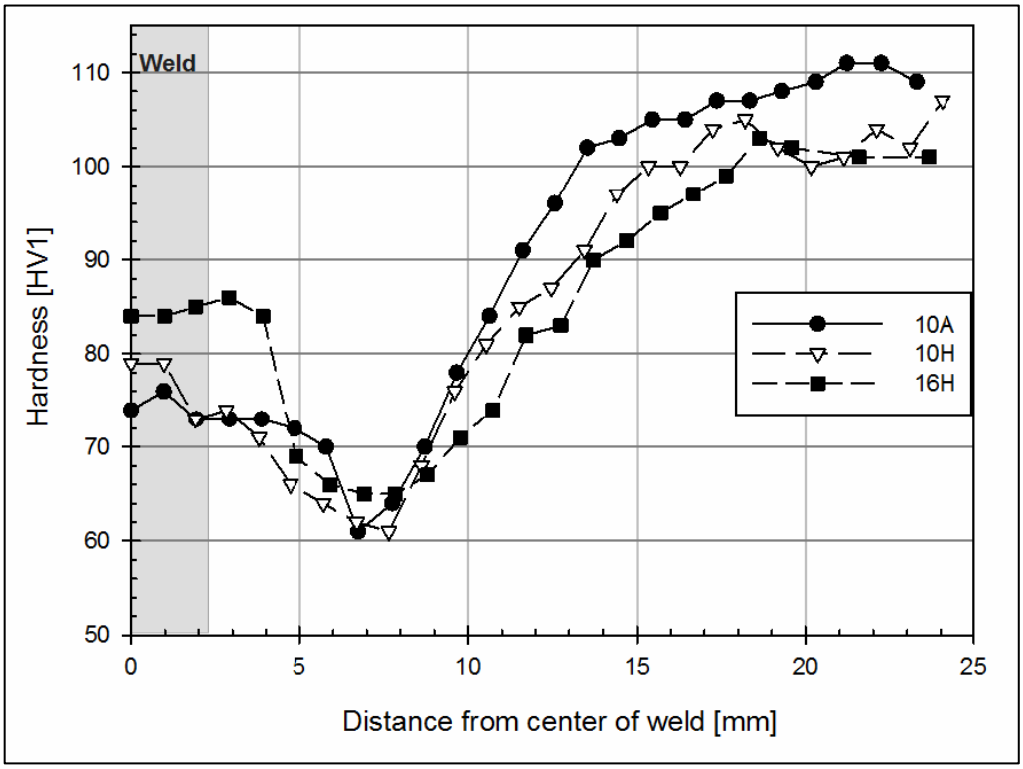

Figure 4.8: Hardness profiles through center of profile for 10A, 10H and 16H

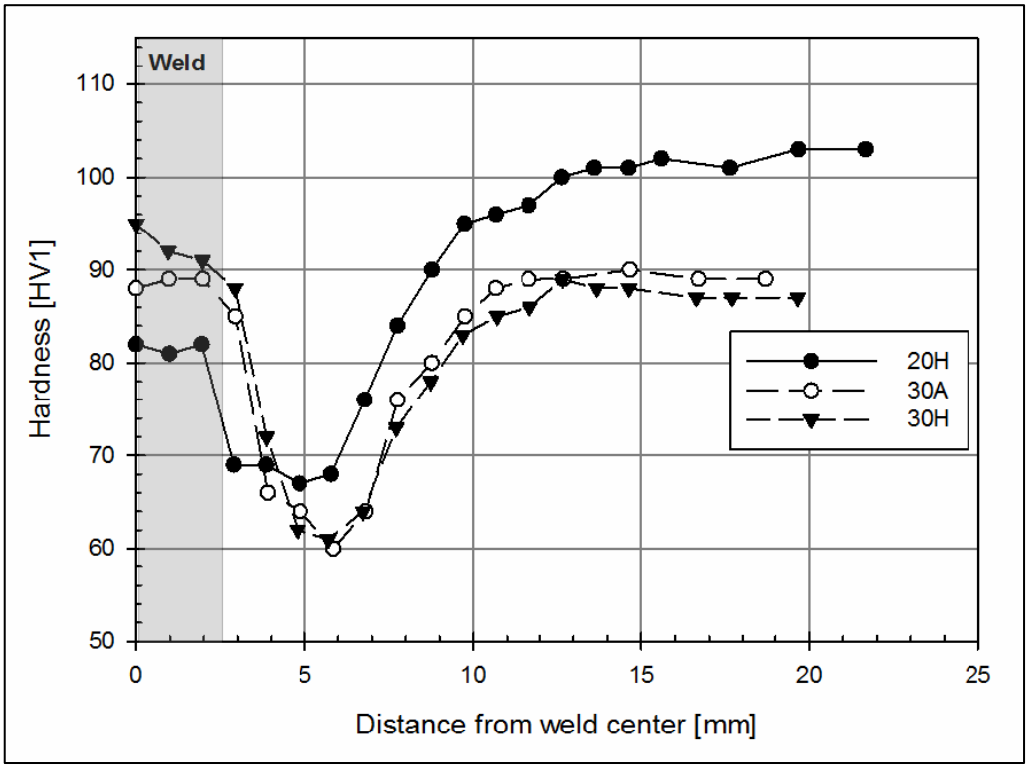

Figure 4.9: Hardness profiles through center of profile for 20H, 30A and 30H

4.1.4 Particle analysis

In Figure 4.10, average particle size represented as spherical diameter for all examined samples is shown. The difference between particle size in base material and the HAZ is negligible as it is within +/- 1 standard deviation, with the exception of the dispersoids in 20H, where the particles are smaller in the HAZ than in base material. The size of the dispersoids seems to be fairly similar for all samples, both in the HAZ and base material. The primary particles in 10H are about 0.75 µm smaller than for the other samples.

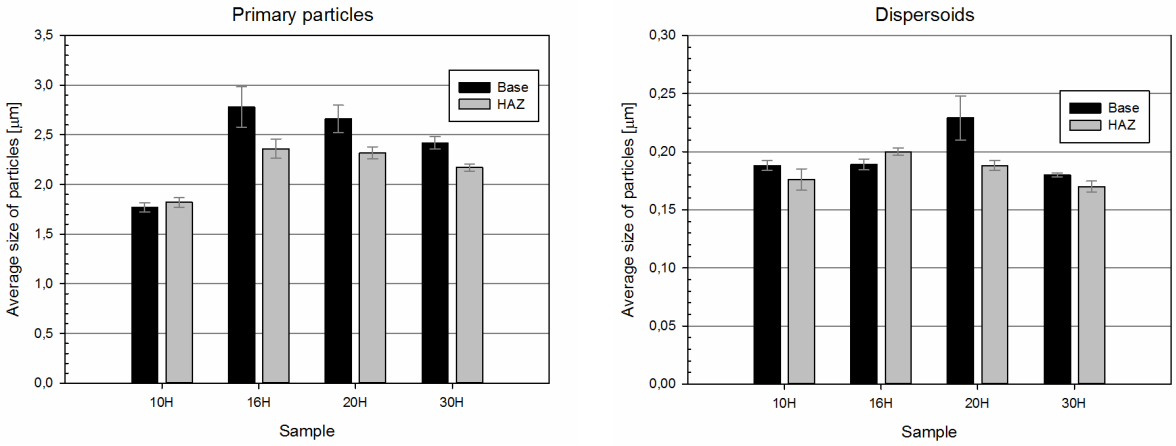

Figure 4.10: Average particle size represented as spherical diameter for primary particles (left) and dispersoids (right) for all examined samples.

In Figure 4.11 the particle density is shown. For primary particles, the density is slightly higher than for the other samples. There is no significant difference between particle density in the HAZ and base material for the primary particles. For the dispersoids, there is also no significant difference between the HAZ and base material, except for 30H, where the dispersoids density is higher in base material than in the HAZ.

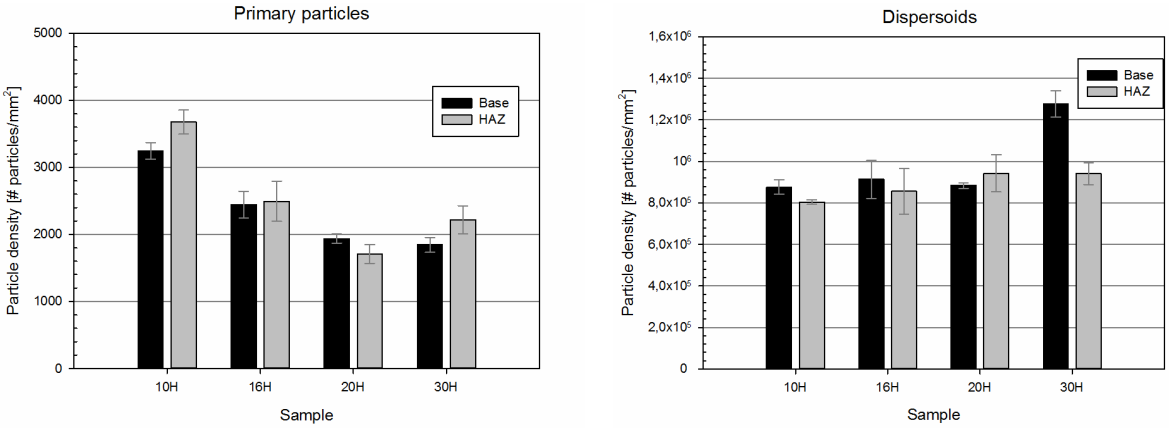

Figure 4.11: Particle density for all examined samples. Primary particles (left) and dispersoids (right).

Figure 4.12 shows the area fraction of primary particles and dispersoids. Almost all measurements have a relatively high standard deviation, so the measurements are not reliable. It should be noted, however, that it may seem like the area fraction in the HAZ is smaller than in base material for dispersoids, as this is true for all samples except 16H.

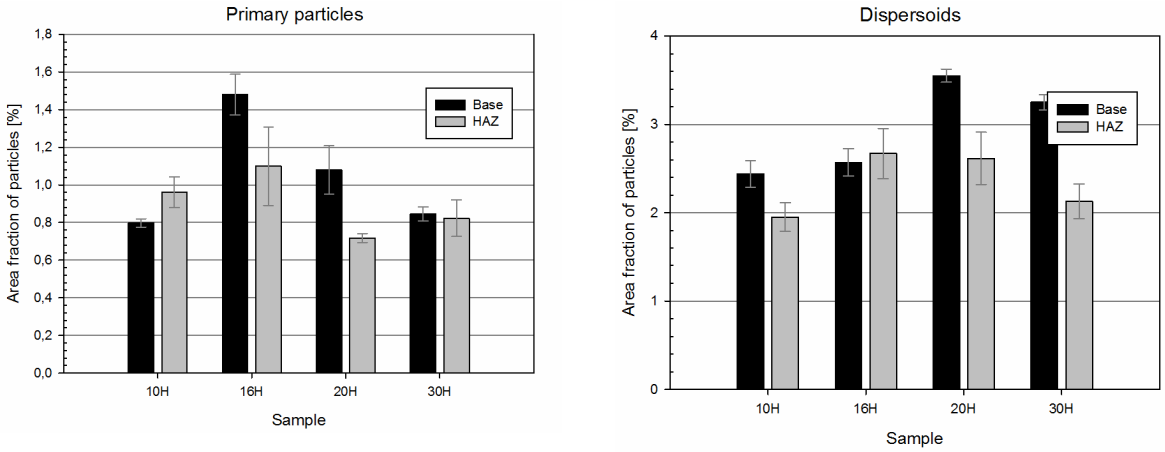

Figure 4.12: Area fraction of particles for all examined samples. Primary particles (left) and dispersoids (right).

Figure 4.13 and Figure 4.14 show the particle size distribution for 10H and 30H, respectively. For 10H, the difference in size distribution is within +/- 1 standard deviation. For 30H, the size distribution in the HAZ is shifted slightly towards the left for primary particles and slightly towards the right for dispersoids. The complete set of size distributions can be found in Appendix F.

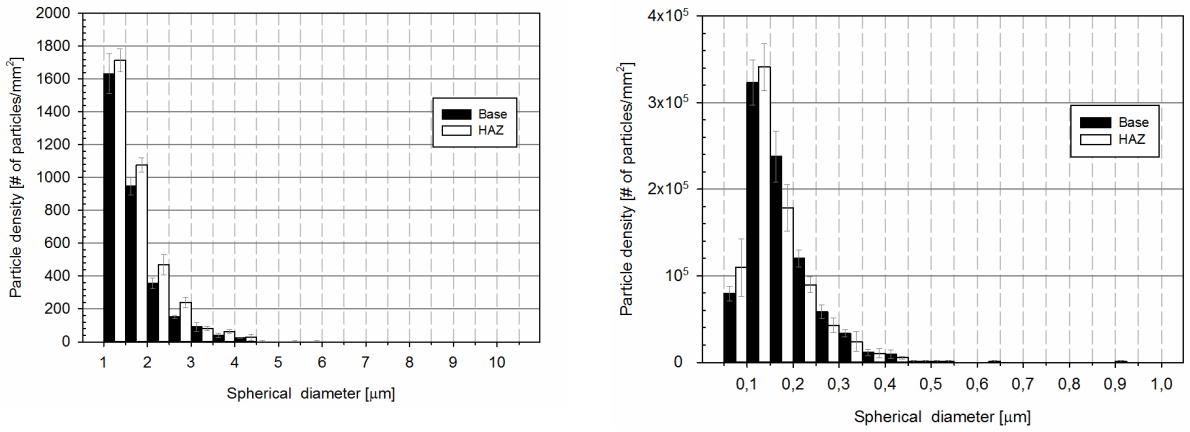

Figure 4.13: Size distribution of primary particles (left) and dispersoids (right) for 10H represented as particle density.

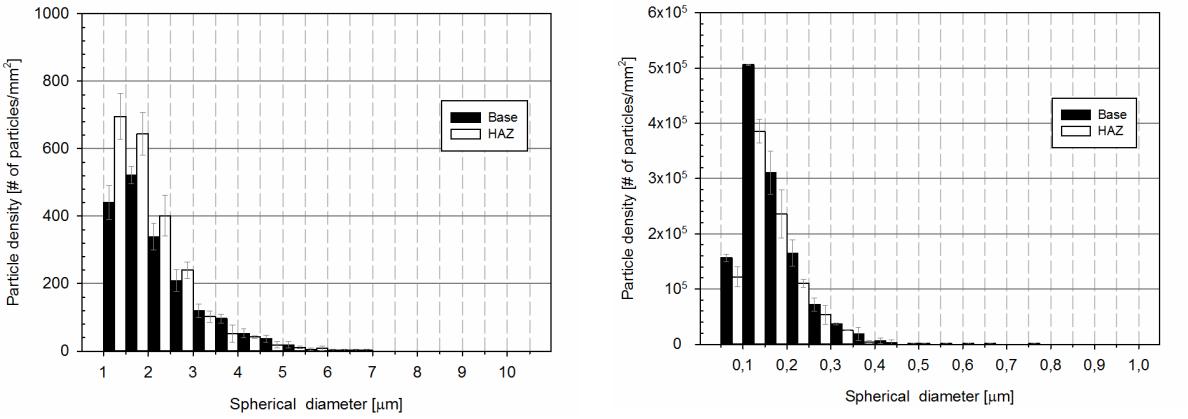

Figure 4.14: Size distribution of primary particles (left) and dispersoids (right) for 30H represented as particle density.

Figure 4.15 show two examples of how the particles appeared in the electron microscope.

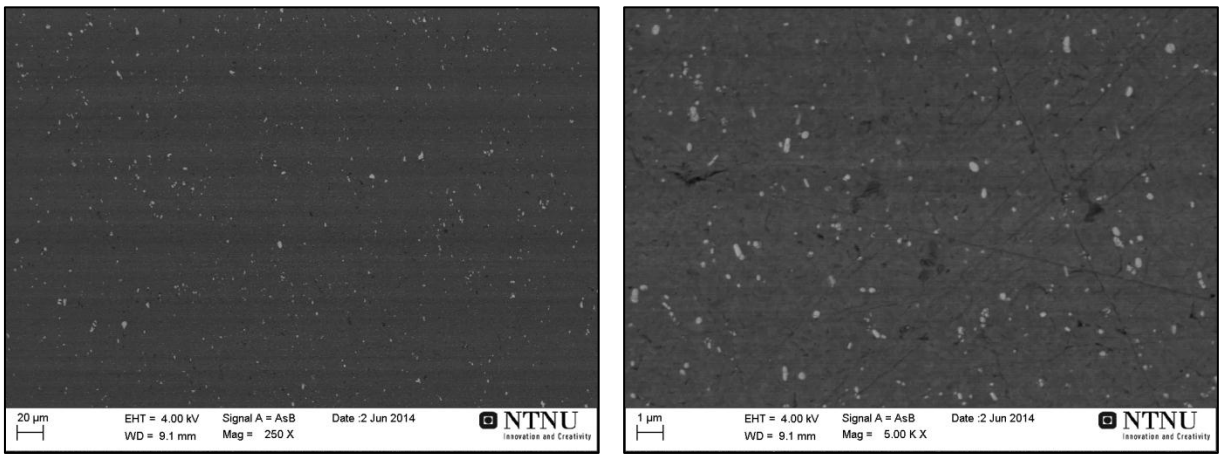

Figure 4.15: Two selected micrographs of primary particles (left) and dispersoids (right) for 10H. Please note difference in scale bar.

4.1.5 Electrical conductivity

The electrical conductivity in base material, HAZ and weld seam is showed in Figure 4.16 where the error bars indicate +/- 1 standard deviation based on three measurements. As can be seen from the figure the HAZ has a slightly higher electrical conductivity than the base material. The weld seam, on the other hand, has about half the electrical conductivity as the base material. All measurements can be found in Appendix F.

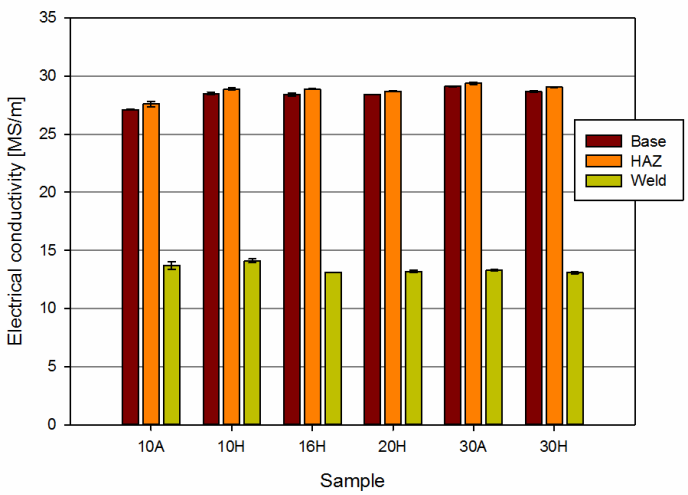

Figure 4.16: Electrical conductivity in base material, HAZ and weld. Error bars indicating +/- 1 standard deviation.

4.2 Corrosion tests

4.2.1 Intergranular corrosion (IGC)

In general, the samples seem to have a low susceptibility to IGC. Some differences between the samples can be seen, however, and in Figure 4.17 the attack density of examined samples is shown. As can be seen, the extrusion plane and the HAZ show very similar attack densities for all samples, whereas the weld has about twice the attack density. However, the attacks on the weld were very shallow as can be seen in Figure 4.18, where the deepest attack is plotted. This figure also shows that the attacks on 20H, 30A and 30H were deeper than on 10A, 10H and 16H.

All the data from Figure 4.17 and Figure 4.18 is based on metallographic examination with the examined plane in parallel with the extrusion direction. For the attack density, all visible attacks were counted.

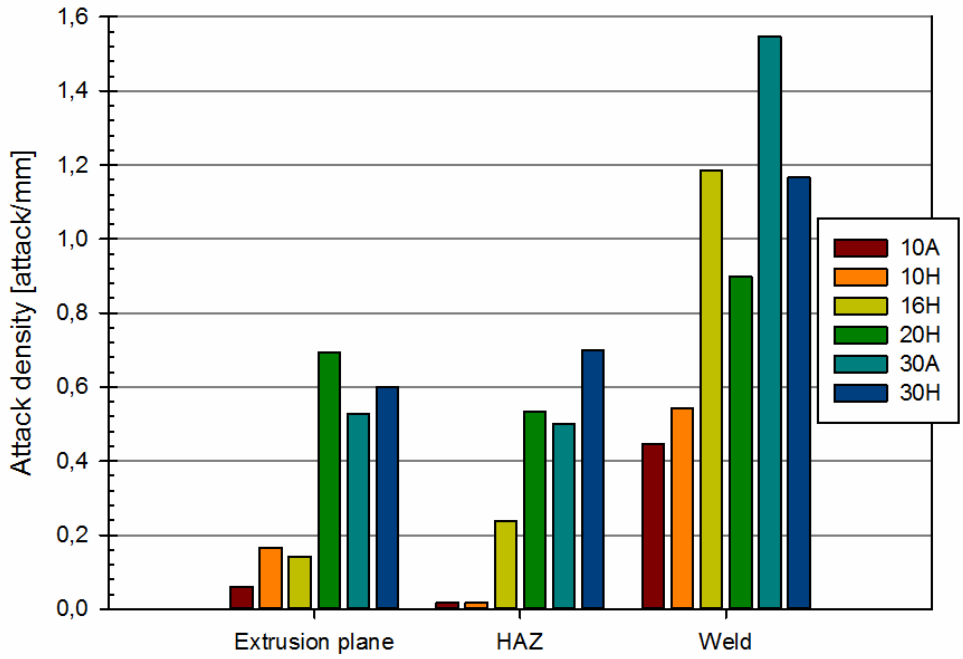

Figure 4.17: Attack density represented as attacks per mm length examined after accelerated IGC test.

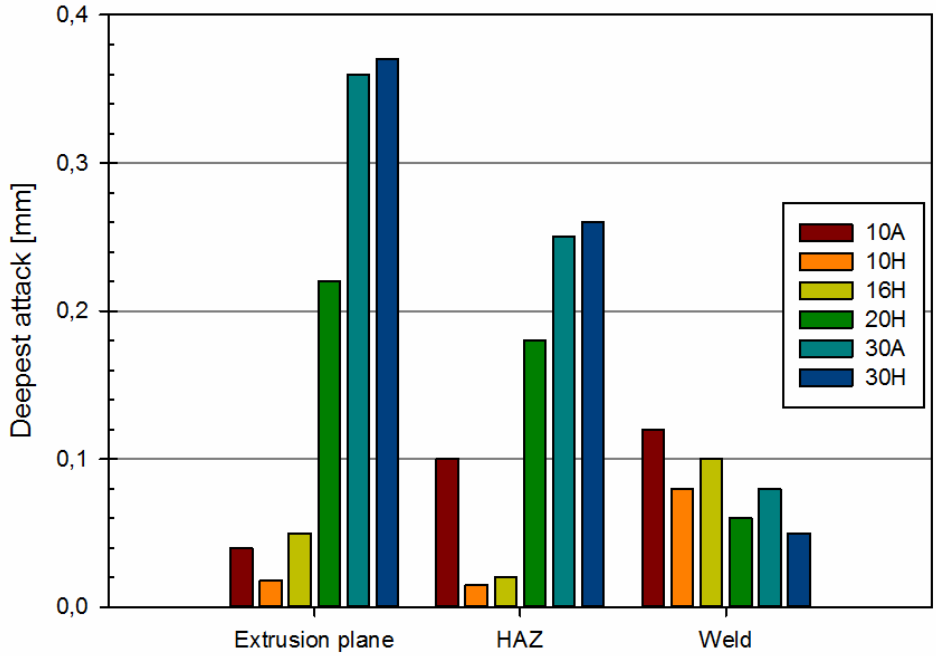

Figure 4.18: Deepest corrosion attack after accelerated IGC test.

A special area of interest is the fusion zone, where the weld and HAZ meet. For the examined samples just 10A, 10H and 16H had attacks here, where 10A had the most severe attack with a depth of 0.55 mm along the fusion zone, as shown in Figure 4.19 A). Given that just a small area of the fusion zone was examined for all samples, it cannot be concluded that the fusion zone for 20H, 30A and 30H will not be susceptible for corrosion attacks here.

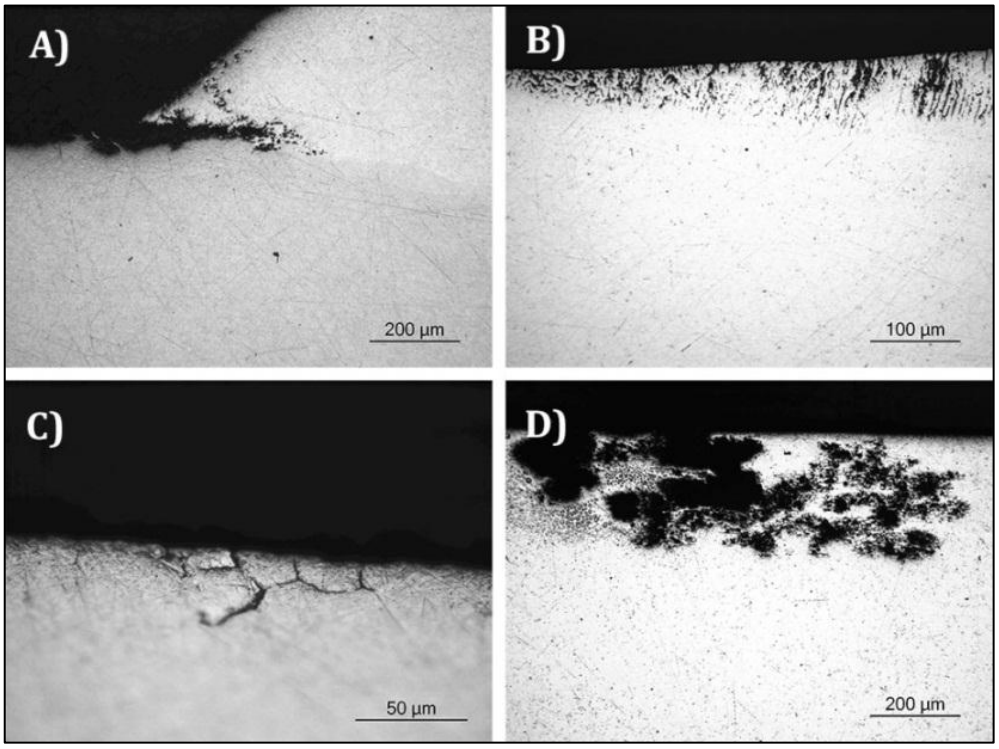

Figure 4.19: Selected optical micrographs of local corrosion attacks. A) Corrosion attack along fusion zone on 10A. B) Wide but shallow corrosion attacks on extrusion plane on 10H. C) Small IGC attack in HAZ on 16H. D) Deep corrosion attack on extrusion plane on 30A. Note difference in scale bars.

4.2.2 Open circuit potential (OCP)

The open circuit potential measured against a standard calomel electrode for base material, HAZ and weld seam over 12 hours is plotted in Figure 4.20, Figure 4.21 and Figure 4.22, respectively. The electrolyte was bubbled with synthetic air. For all regions, a lowering of the temperature from 25 °C to 2 °C gave a rise in the open circuit potential of about 100-200 mV. The unstable nature of aluminium alloys is also evident, as the measurements are not stable. However, the measurements at 2 °C always lie above the 25 °C measurements. It may also seem like the OCP for the weld is slightly higher than in the HAZ. The measurements in the HAZ and base material are very similar for both high and low temperature.

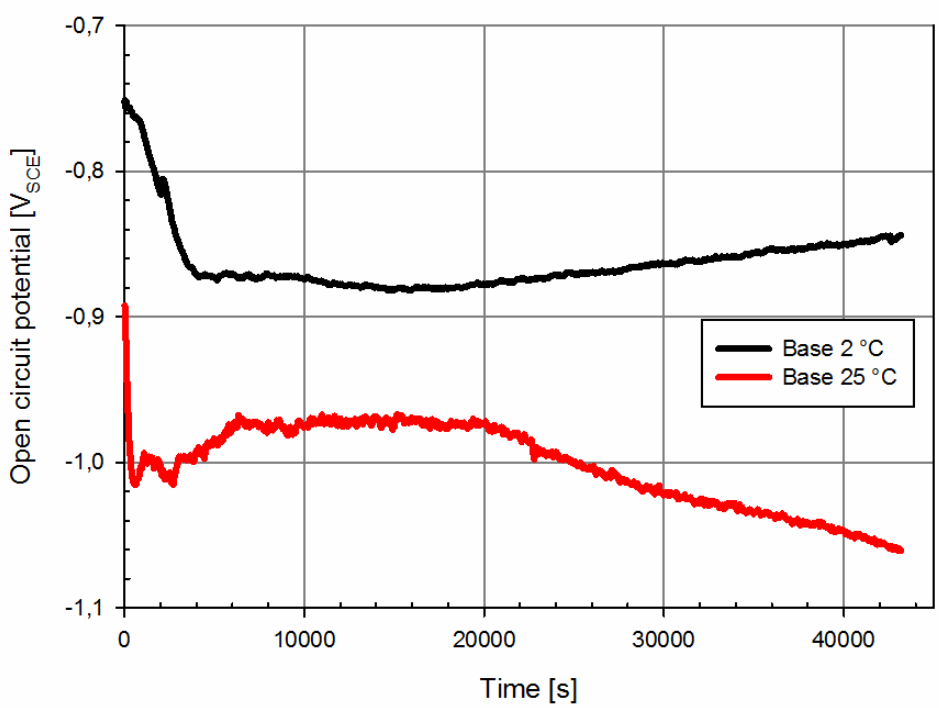

Figure 4.20: Open circuit potential in artificial seawater bubbled with synthetic air over the course of 12 hours for base material of 30H.

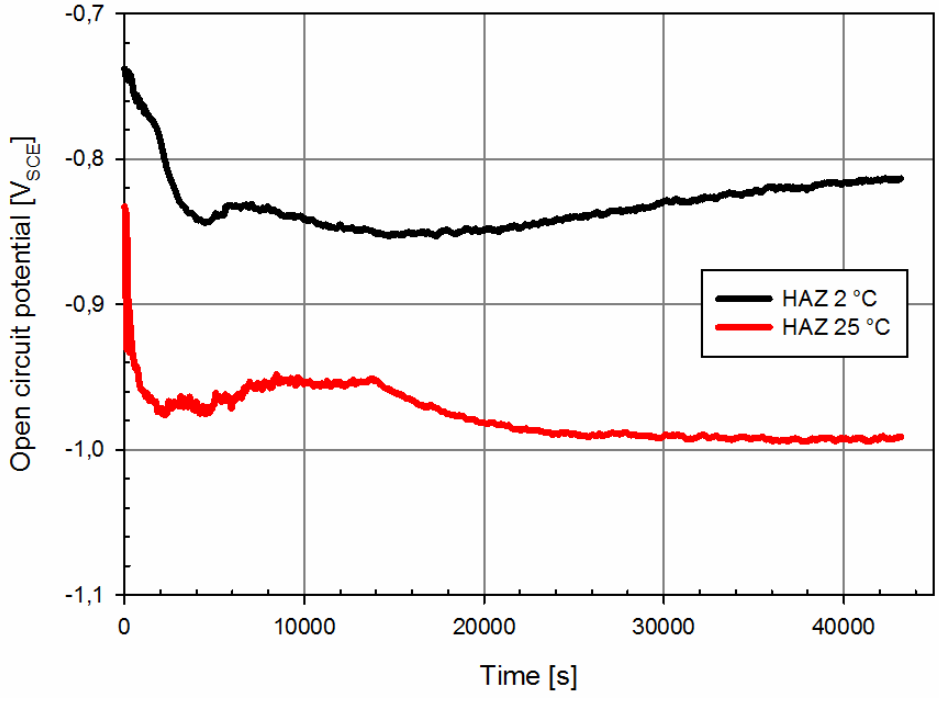

Figure 4.21: Open circuit potential in artificial seawater bubbled with synthetic air over the course of 12 hours for the HAZ of 30H.

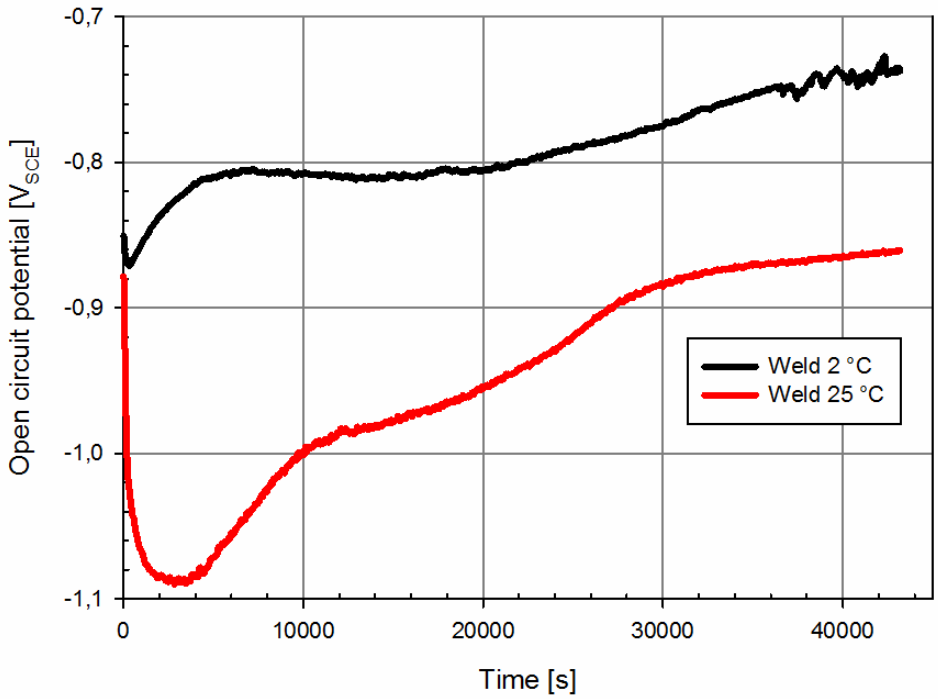

Figure 4.22: Open circuit potential in artificial seawater bubbled with synthetic air over the course of 12 hours for the weld of 30H.

4.2.3 Polarization curves

All parallels of the recorded polarization curves for high and low temperature with the electrolyte bubbled with synthetic air and nitrogen gas, are shown in Figure 4.23 and Figure 4.24, respectively. A lowering of the temperature from 25 °C to 2 °C rises the corrosion potential with about 0.1 V for an electrolyte saturated with dissolved oxygen and 0.15 V for an electrolyte depleted of dissolved oxygen. A lower temperature also seems to lower the limiting cathodic current and raise the pitting potential. The main corrosion parameters are summarized in Table 4.3.

Table 4.3: Average main corrosion parameters based on the three parallels.

Temperature	Electrolyte	E_{corr} [V]	$E_{pitting}$ [V]	i_{lim} [µA/cm^2] at -1.1 V
25 °C	Saturated	-0.831	-0.730	17
2 °C	Saturated	-0.738	-0.591	7.5
25 °C	Depleted	-0.909	-0.714	25
2 °C	Depleted	-0.741	-0.688	33.5

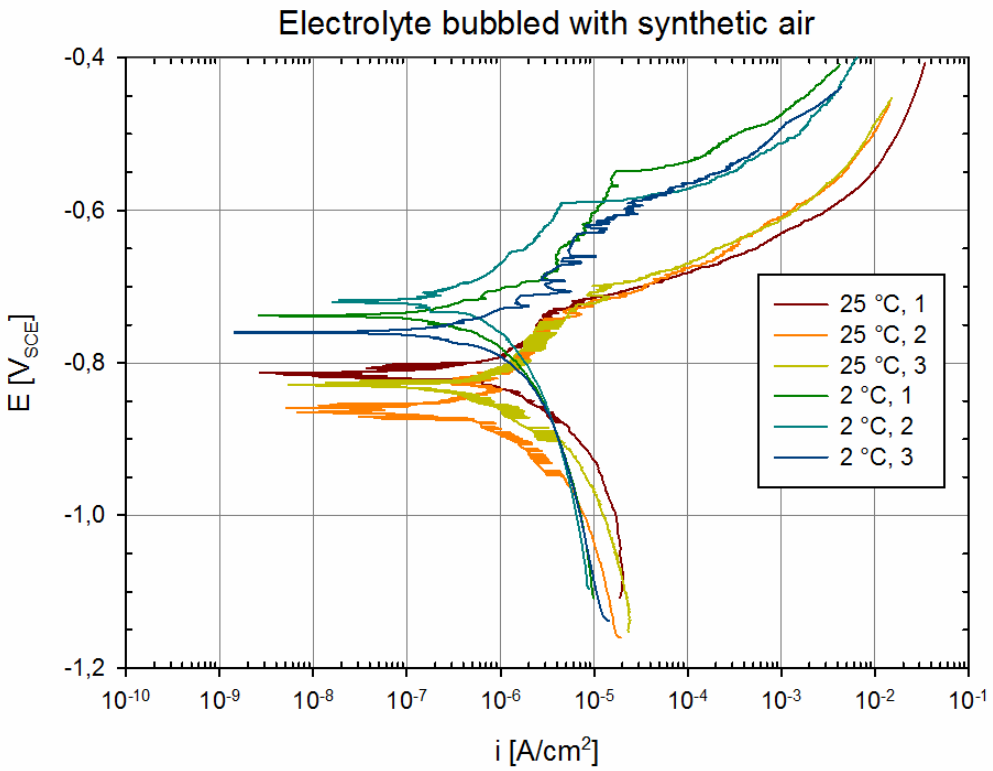

Figure 4.23: Polarization curves at 25 and 2 °C. Electrolyte bubbled with synthetic air.

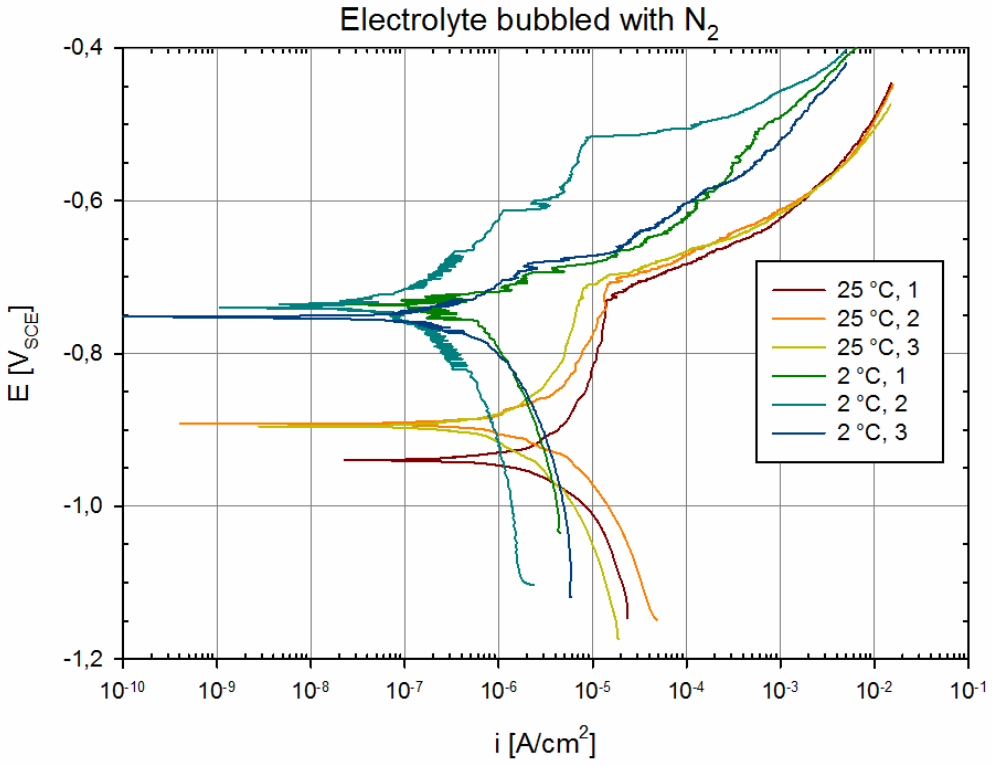

Figure 4.24: Polarization curves at 25 and 2 °C. Electrolyte bubbled with N_2.

4.3 Weld simulations

4.3.1 Hardness

In Figure 4.25, the hardness profiles for the weld simulated samples are presented. As can be seen from the figure, all samples had a minimum hardness very close to the thermo element, except sample 530. The minimum hardness and the corresponding point in the welded samples based on hardness are listed in Table 4.4.

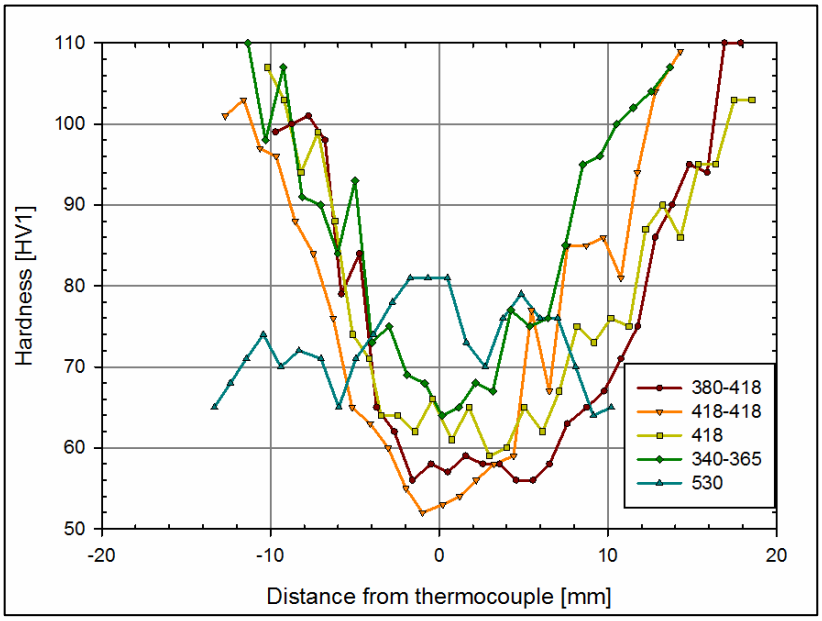

Figure 4.25: Hardness profiles of weld simulated samples.

Table 4.4: Minimum hardness and corresponding position in the welded samples for the weld simulated samples.

Sample	Minimum hardness [HV1]	Corresponding position in welded samples
380-418	58	HAZ, minimum hardness
418-418	53	Softer than minimum hardness
418	61	HAZ, minimum hardness
340-365	64	HAZ, but not minimum hardness
530	81 (at thermocouple)	Fusion line

4.3.2 Tensile tests

A summary of the tensile tests for all samples is listed in Table 4.5 and the stress-strain curves can be seen in Figure 4.26. As can be seen, the two parallels for all samples were very similar. A closer look at the table reveals that the extra heat cycle up to 380 °C in the 380-418 sample led to a weakening of the yield strength of about 14 N/mm^2 compared to the 418 sample. The extra heat cycle up to 418 °C

in the 418-418 sample led to a further weakening of the yield strength of about 17 N/mm^2 compared to the 418 sample.

For the 530 sample, the necking started outside the extensometer. This means that the weakest position of the material was not were the thermocouple was placed during simulations. This was expected from the hardness samples, but means that the tensile test for this sample will not be valid as it will not reflect the position in the HAZ that was intended.

Table 4.5: Summary of results from tensile tests of weld simulated samples.

Sample	Area [mm^2]	$R_{p0.2}$ [N/mm^2]	R_m [N/mm^2]	Strain at yield [%]	E-module [GPa]
Control (1)	11.9	328.5	349.2	0.656	72.896
Control (2)	11.7	325.4	345.0	0.654	72.631
380-418 (1)	11.8	143.3	215.8	0.392	74.462
380-418 (2)	11.9	136.3	209.6	0.402	70.145
418 (1)	11.7	152.1	225.4	0.409	73.712
418 (2)	11.8	156.9	228.2	0.432	68.529
418-418 (1)	11.9	136.0	212.5	0.394	69.9
418-418 (2)	12.0	138.8	213.3	0.394	72.4
340-365 (1)	12.0	197.7	240.2	0.482	70.192
340-365 (2)	12.1	191.2	235.3	0.477	71.419
530 (1)	12.1	151.0	224.3	0.413	70.393
530 (2)	11.7	153.9	224.7	0.427	73.292

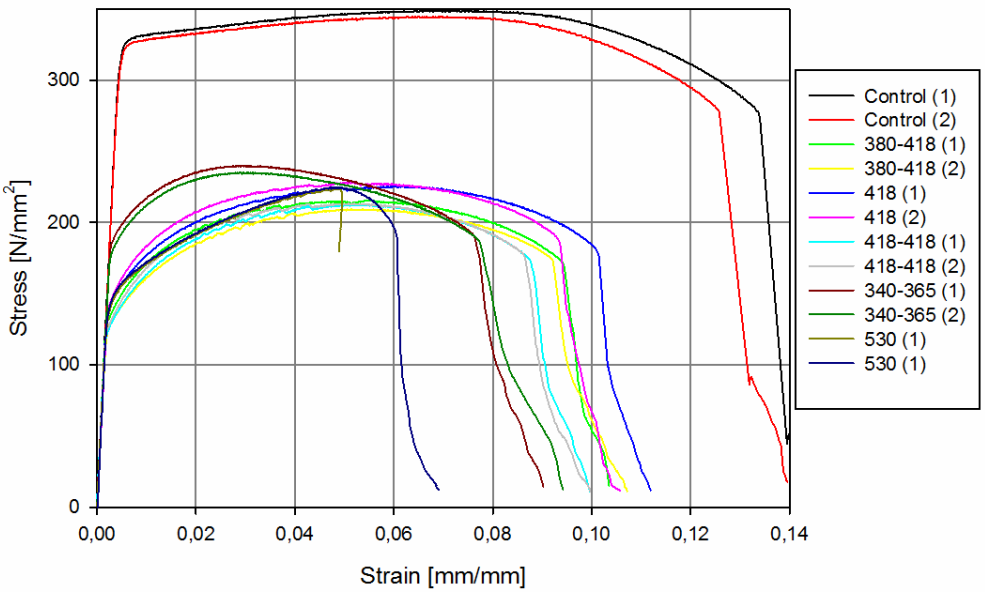

Figure 4.26: Stress-strain curves from tensile testing of weld simulated samples.

5 Discussion

5.1 Material characterization

In this section the most important aspects of the material characterization will be discussed in some further detail.

5.1.1 Microstructure

It is evident from the micrographs in section 4.1.2 that the recrystallized layer decreases as the thickness of the profile increases. This is caused by a smaller strain for the thicker profiles as the reduction of area is smaller during extrusion. Smaller strain means smaller dislocation density and hence smaller driving force for recrystallization, as discussed in section 2.2.

The micrographs of the cross section of the weld 10A and 10H in Figure 4.5 reveal that the recrystallized layer decreases towards the weld bead. This is probably caused by grinding of the surface prior to welding. This is done to prepare the surface and remove any oxide layer that may have been formed between extrusion and welding. It is important to be aware of this as the removal of the recrystallized layer may have implications on the corrosion behaviour.

5.1.2 Hardness profiles

The hardness profiles through the weld cross section are in accordance to the strength evolution during welding discussed in section 2.4.1. The hardness decreases with increasing distance from the weld center line until a minimum hardness is reached after about 5-7 mm, dependent on the profile thickness.

The hardness of the weld seems to increase as the number of weld layers increases. This may be caused by the reheating of the weld layers as new layers are added and causes precipitation of MgSi-particles. This effect will, however, not affect the outermost layers, but is evident in the hardness profiles for this study as they are measured through the profile center line, i.e. the inner most weld layers.

5.1.3 Particle analysis

It was not expected that the particle size and density would change in the HAZ compared to the base material. Primary particles are formed during casting and the heat cycles during welding are not sufficient to give any coarsening or dissolution of the dispersoids. During extrusion, the primary particles will experience some deformation as the reduction of thickness can be substantial. This will have a greater impact on the thinner profiles as they experience more a higher strain. As the primary particles in the 10 mm profile are smaller and have higher density than the other profiles, it is

reasonable to assume that deformation and breaking of primary particles has happened for this thickness, but not for the other profiles.

The dispersoid size in 20H has an abnormity compared to the other as it is bigger in base material than in HAZ. It can also be seen that the standard deviation in much bigger for this than for the others. This can then probably be explained by the variations in settings for threshold, contrast and brightness during analysis and is therefore a false result. The same is also true for the dispersoids density in 30H. These false results also lead to false results in the area fraction of dispersoids as seen in Figure 4.12, for the mentioned samples.

5.1.4 Electrical conductivity

The electrical conductivity measurements showed that the HAZ has a slightly higher conductivity than base material. This is due to precipitation from solid solution during the welding heat cycle. Less alloying elements in solid solution will increase the electrical conductivity by making it easier for the electrons to move as the elastic stress field caused by elements in solid solution will be less dominant. This is in accordance with the microstructure evolution during welding discussed in 2.4.1.

The weld displayed an electrical conductivity of just half of the base material. As the weld has an as-cast microstructure, it will have more elements in solid solution and thereby giving poor electrical properties.

5.2 Corrosion tests

In this section the results from the corrosion tests will be discussed in further detail.

5.2.1 Intergranular corrosion (IGC)

The accelerated intergranular corrosion test showed differences in corrosion behaviour for the different samples that can be explained by the differences in microstructure. A fibrous microstructure is generally regarded as beneficial and M. H. Larsen[22] showed that a IGC attacks are often limited to the recrystallized layer and do not penetrate the fibrous microstructure, when such a layer exists. As the deepest attacks on the 10 and 16 mm profiles where not deeper than the thickness of the recrystallized layer, the results provided by Larsen are also valid in this study. The deepest attacks on the 20 and 30 mm profile, however, were much deeper than their very limited recrystallized layer, and also much deeper than the thinner profiles. This suggests that the transition from a recrystallized to a fibrous microstructure acts as a barrier for further propagation of IGC attacks. And that a combination of microstructures can be beneficial. The mechanisms behind this barrier were not examined. It is reasonable, however, to believe that this is linked to the distribution of alloying elements during recrystallization, as IGC is often linked to the distribution of Cu-rich phases on the grain boundaries.

The HAZ seems to have less susceptibility to IGC than the base material as both the attack density and deepest attack is smaller for all samples. It should also be mentioned that the relatively deep attack in the HAZ of 10A can be explained by the removal of the recrystallized layer prior welding, exposing the fibrous structure. The improved IGC resistance in HAZ is probably linked to the coarsening of the grain boundary phases. The weld bead had a fairly high corrosion attack density for all samples, but the attacks were very limited in depth. This means that intergranular corrosion will probably not be crucial for the weld bead properties.

Deep corrosion attacks on the fusion line between the weld bead and HAZ were found on some samples as shown in Figure 4.19, after the accelerated IGC test. This can be caused by potential differences between the weld and HAZ and thereby a galvanic coupling can be established giving galvanic corrosion. This will be discussed further in the following section.

5.2.2 Open circuit potential

As seen in section 4.2.2, a lowering of the temperature from 25 °C to 2 °C results in a raising of the open circuit potential of 100-200 mV for all examined regions. As the base material and HAZ has the same chemical content, the open circuit potential for these regions was expected to be very similar. The measurements showed that this was true at both 25 °C and 2 °C.

A compiled plot of the open circuit potential for HAZ and weld seam is showed in Figure 5.1. As can be seen from this figure, the instability of the OCP causes the difference between the two regions to alter, but it may seem like the HAZ has a more negative OCP than the weld at steady state. This can cause galvanic corrosion between the HAZ and weld and may also explain the deep corrosion attacks observed between these two regions after the accelerated IGC test. This is of major importance as a weakening in this region is detrimental to the mechanical properties of the weld as it is the weakest region of the profile. This underlines the importance of the choice of filler wire during welding. It should be noted however, that the difference in OCP is not very large. It is often said that a difference of 100 mV must be present to achieve galvanic corrosion.[53]

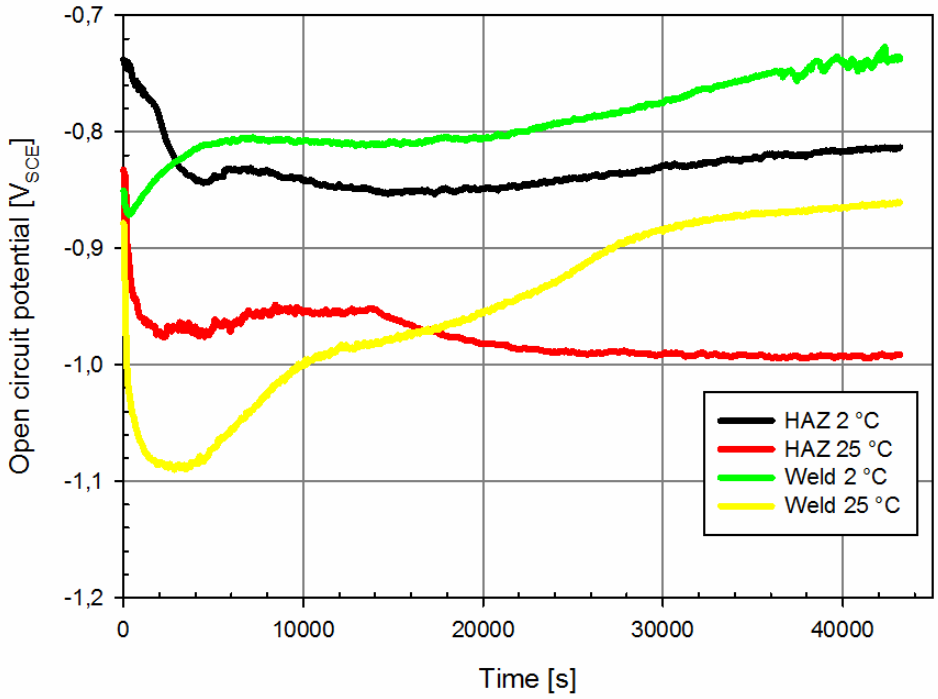

Figure 5.1: Compiled plot of open circuit potential of HAZ and weld seam.

5.2.3 Polarization curves

The polarization curves shown in Figure 4.23 and Figure 4.24 clearly demonstrate that the effect of lowering the temperature will be beneficial for the corrosion behaviour of the examined aluminium alloy. This can be seen by the raising of the corrosion potential of about 100-180 mV, the lowering of the limiting cathodic current and the raising of the pitting potential. As discussed in section 2.5.3, this is probably due to slower diffusion of oxygen, lower amount of dissolved oxygen at lower temperatures and lower hydration degree of the oxide film. The results from this study are then in accordance to the literature discussed in this section.

The difference in corrosion potential between high and low temperature is more evident for the electrolyte bubble with N_2. This is due to that the corrosion potential at 25 °C is about 80 mV lower for the electrolyte depleted with oxygen, whereas the corrosion potential is about the same at 2 °C for the different electrolytes. It should be noted, however, that the electrolyte bubbled with N_2 was probably not completely depleted of oxygen as the test cell was not completely air tight. This means that some oxygen may have diffused into the electrolyte.

5.3 Weld simulations

To evaluate the weld simulations, they can be compared to the tensile tests over the weld performed by Hydro, given in Table 5.1. This shows that the parent material had very similar yield and ultimate

tensile strength, which shows that the tests were carried out in a way so that they can be compared. The 380-418 sample was intended to simulate the position of minimum strength in the weld and had a yield strength of 140 MPa. The welded sample, on the other hand, had a tensile strength of 181.3 MPa. It is possible that the weld simulated samples did not have time to natural age to peak hardness, as the tensile tests were carried out four weeks after simulations. The hardness measurements confirms that the simulations produced a strength lower than in the welded samples, as the hardness at the thermo element for the 380-418 sample was lower than in the minimum hardness in the HAZ.

Table 5.1: Tensile test performed by Hydro of parent material and weld.

Sample material	$R_{p0.2}$ [N/mm^2]	R_m [N/mm^2]
Parent	322.4	345.1
Weld	181.3	259.6

The tensile tests also show that the strength of the HAZ is highly dependent on the peak temperature in the weld heat cycles. This is evident as the strength decreases as the peak temperature increases or the number of heat cycles increase for the 418, 418-418 and 380-418 samples. Higher peak temperature and higher number of heat cycles will probably increase the coarsening of the hardening precipitates as reviewed in section 2.4.1, and thereby give lower strength. Sample 530 showed a higher tensile strength than sample 418. This is caused by that at this temperature the precipitates will dissolve and natural ageing will reproduce some of the strength lost.

5.4 Further work

Further work should include a more comprehensive study of the effect of low temperature on mechanical properties, e.g. fatigue, creep and fracture toughness, in both parent material and welded profiles. By performing such tests at low temperatures, it will lead to a better understanding of the possibilities for use of aluminium in the arctic region. Also, corrosion tests at intermediate temperature can be done to produce a full understanding of the effect of low temperatures and it may also lead to a correlation between temperature and corrosion rate. In addition, effect of the extremely low temperatures that will be encountered for top side structures (< -60 °C), especially in the splash zone, should be studied.

Moreover, the effect of a recrystallized layer on IGC and pitting is not fully understood. More comprehensive studies of the grain boundary intermetallic phase particles on the transition between recrystallized and fibrous microstructure may lead to a better understanding. This can be done by transmission electron microscopy (TEM) and X-ray diffraction (XRD). A comparison between the susceptibility to IGC and pitting at high and low temperatures may also lead to a better understanding of how the corrosion behaviour of aluminium alloys will be in the arctic region.

Finally, a comparison study between different mixtures of aluminium alloys and filler wire, with regards to corrosion behaviour may lead to better knowledge of what filler wires should be used to weld different alloys.

6 Conclusions

This master thesis has studied the effect of welding on mechanical properties and corrosion behaviour of extruded AA6082 profiles. In addition the effect of low temperature on corrosion has been studied. Main conclusions that can be drawn from this study are as follows:

- The mechanical properties of extruded 6082-T6 aluminium weldments do not change when the thickness of the profiles and number of weld layers increase up to a thickness of 30 mm. As a result of this, it is recommended to include profiles with a thickness up to 30 mm in EN 1999-1-1[1].
- The HAZ in the examined profiles is not more susceptible to IGC than the base material. Although the attack density of the weld bead was fairly high, these attacks were very limited in depth.
- The transition from a recrystallized to a fibrous microstructure seems to create a barrier towards further propagation of IGC attacks. Care must therefore be taken to not remove the recrystallized layer as a result of grinding prior to welding. The mechanisms behind this barrier is not fully understood, but may be linked to the distribution of alloying elements in solid solution and intermetallic particles during recrystallization.
- Care must also be taken when selecting filler wire as there is a possibility for galvanic corrosion between the weld and HAZ. The results from this study, however, showed just a slightly higher OCP for the weld than in the HAZ.
- The low ocean temperatures that will be encountered in the arctic region should not propose any danger towards the corrosion resistance. This is shown by an increase of the corrosion and pitting potential and a lowering of the cathodic limiting current. The improved corrosion resistance at low temperatures can be explained by the slower rate of dissolution of the protective layer, slower diffusion of oxygen, lower hydration degree of the oxide film and lower concentration of oxygen.
- Weld simulations showed that the effect of multi-pass welding is dependent on the peak temperature of all layers, not just the highest. This was showed by that the addition of a 380 °C heat cycle to a 418 °C heat cycle led to a further weakening of the yield strength of 14.7 MPa. And two 418 °C heat cycles gave a yield strength 20.1 MPa lower than a single 418 °C heat cycle.

7 References

1. CEN, *Eurocode 9: Design of aluminium structures*, in *Part 1-1: General structural rules*. 2007, EN 1999-1-1:2007+A1.
2. Myhr, O.R. and Ø. Grong, *Novel modelling approach to optimisation of welding conditions and heat treatment schedules for age hardening Al alloys.* Science and Technology of Welding and Joining, 2009. **14**(4): p. 321-332.
3. SINTEF. *Arctic Materials*. April 6, 2011 [cited 2013 5. dec]; Available from: http://www.sintef.no/Projectweb/Arctic-Materials/.
4. Institute, T.I.A. *Aluminium for future generations*. 2012 [cited 2013 5. dec]; Available from: http://recycling.world-aluminium.org/home.html.
5. Reiso, O., *Extrusion of AlMgSi Alloys.* Materials Forum, 2004. **28**: p. 32-46.
6. Solberg, J.K., *Teknologiske metaller og legeringer*. 2010, Institutt for materialteknologi: NTNU. p. 200-218.
7. Zhang, J., et al., *Equilibrium pseudobinary Al-Mg2Si phase diagram.* Materials Science and Technology, 2001. **17**(5): p. 494-496.
8. Reiso, O., *Extrusion and Al Metallurgy*, in *Lecture notes*. 2013, NTNU.
9. F.J. Humphreys, M.H., *Recrystallization and Related Annealing Phenomena*. 2004, Elsevier. p. 269-283.
10. Myhr, O., Ø. Grong, and K. Pedersen, *A Combined Precipitation, Yield Strength, and Work Hardening Model for Al-Mg-Si Alloys.* Metallurgical and Materials Transactions A, 2010. **41**(9): p. 2276-2289.
11. Myhr, O., et al. *Modeling of microstructure evolution and residual stresses in processing and welding of 6082 and 7108 aluminium alloys*. in *5th International Conference on Trends in Welding Research, Pine Mountain, Georgia, USA*. 1998.
12. Myhr, O.R., et al., *Modelling of the microstructure and strength evolution in Al–Mg–Si alloys during multistage thermal processing.* Acta Materialia, 2004. **52**(17): p. 4997-5008.
13. Marioara, C.D., et al., *The effect of Cu on precipitation in Al–Mg–Si alloys.* Philosophical Magazine, 2007. **87**(23): p. 3385-3413.
14. Grong, Ø., *Recent Advances in Solid-State Joining Of Aluminum.* Welding Journal, JAN 2012. **91**(1): p. 26-33.
15. Wolverton, C., *Crystal structure and stability of complex precipitate phases in Al–Cu–Mg–(Si) and Al–Zn–Mg alloys.* Acta Materialia, 2001. **49**(16): p. 3129-3142.
16. Mondolfo, L.F., *Aluminium Alloys: Structure and Properties*. 1976: Butterworths.
17. Larsen, M.H., et al., *Intergranular Corrosion of Copper-Containing AA6xxx AlMgSi Aluminium Alloys.* Journal of the Electrochemical Society, 2008. **155**(11): p. C550-C556.
18. Akselsen, O.M., *Joining Technology*. 2012, NTNU: Trondheim, Norway.
19. Mathers, G., *Welding of Aluminium and Its Alloys*. 2002, Boca Raton, USA: Woodhead Publishing Ltd.
20. M., M.W.A.a.M., *Susceptibility of some 6000 Al weldments to pitting and intergranular corrosion*. Vol. 50. 1996, Hannover, ALLEMAGNE: Giesel.
21. Myhr, O.R., *Process Modelling Applied to 6082-T6 Aluminium Weldments*. 1990: Metallurgisk Institutt, NTNU. p. 59.
22. Larsen, M.H., *Effect of composition and thermomechanical processing on the intergranular corrosion of AA6000 aluminium alloys*. Vol. 2010:116. 2010, Trondheim: Norges teknisk-naturvitenskapelige universitet. VI, 103 s. : ill.
23. Larsen, M.H., et al., *Effect of Excess Silicin and Small Copper Content on Intergranular Corrosion of 6000-series Aluminium Alloys.* Journal of The Electrochemical Society, 2010. **157**(2): p. C61-C68.

24. Svenningsen, G., et al., *Effect of high temperature heat treatment on intergranular corrosion of AlMgSi(Cu) model alloy.* Corrosion Science, 2006. **48**: p. 258-272.
25. Svenningsen, G., et al., *Effect of thermomechanical history on intergranular corrosion of extruded AlMgSi(Cu) model alloy.* Corrosion Science, 2006. **48**: p. 3969-3987.
26. Svenningsen, G., et al., *Effect of artificial aging on intergranular corrosion of extruded AlMgSi alloy with small Cu content.* Corrosion Science, 2006. **48**: p. 1528-1543.
27. Galvele, J.R. and S.M. de De Micheli, *Mechanism of intergranular corrosion of Al-Cu alloys.* Corrosion Science, 1970. **10**(11): p. 795-807.
28. Minoda, T. and H. Yoshida, *The Effect of Microstructure on Intergranular Corrosion Resistance og 6061 Alloy Extrusion.* Materials Science Forum, 2000. **331-337**: p. 1689-1694.
29. Muller, I.L. and J.R. Galvele, *Pitting potential of high purity binary aluminium alloys—I. Al‐Cu alloys. Pitting and intergranular corrosion.* Corrosion Science, 1977. **17**(3): p. 179-193.
30. Svenningsen, G., et al., *Effect of low copper content and heat treatment on intergranular corrosion of model AlMgSi alloys.* Corrosion Science, 2006. **48**: p. 226-242.
31. Wang, Z., et al., *Improving the intergranular corrosion resistance of Al–Mg–Si–Cu alloys without strength loss by a two-step aging treatment.* Materials Science and Engineering: A, 2014. **590**(0): p. 267-273.
32. Zeng, F.-l., et al., *Corrosion mechanism associated with Mg2Si and Si particles in Al–Mg–Si alloys.* Transactions of Nonferrous Metals Society of China, 2011. **21**(12): p. 2559-2567.
33. Zhan, H., et al., *The influence of copper content on intergranular corrosion of model AlMgSi(Cu) alloys.* Materials and Corrosion, 2008. **59**(8): p. 670-675.
34. El-Menshawy, K., et al., *Effect of aging time at low aging temperatures on the corrosion of aluminum alloy 6061.* Corrosion Science, 2012. **54**(0): p. 167-173.
35. Ezuber, H., A. El-Houd, and F. El-Shawesh, *A study on the corrosion behaviour of aluminum alloys in seawater.* Materials & Design, 2008. **29**(4): p. 801-805.
36. Frankel, G.S., *Pitting Corrosion of Metals - A review of Critical Factors.* Journal of the Electrochemical Society, 1998. **145**(6): p. 2186-2198.
37. Liang, W.J., et al., *General aspects related to the corrosion of 6xxx series aluminium alloys: Exploring the influence of Mg/Si ratio and Cu.* Corrosion Science, 2013. **76**(0): p. 119-128.
38. Muller, I.L. and J.R. Galvele, *Pitting potential of high purity binary aluminium alloys—II. AlMg and AlZn alloys.* Corrosion Science, 1977. **17**(12): p. 995-1007.
39. Pride, S.T., J.R. Scully, and J.L. Hudson, *Metastable Pitting of Aluminum and Criteria for the Transition to Stable Pit Growth.* Journal of The Electrochemical Society, 1994. **141**(11): p. 3028-3040.
40. Szklarska-Smialowska, Z., *Pitting corrosion of metals*, in *NACE*. 1986: Houston, Texas. p. 223-2240.
41. Vargel, C., M. Jacques, and M.P. Schmidt, *Types of Corrosion on Aluminium*, in *Corrosion of Aluminium*, C. Vargel, M. Jacques, and M.P. Schmidt, Editors. 2004, Elsevier: Amsterdam. p. 113-146.
42. Kjetil S. Rostad, T.F., Otto Lunder, *Corrosion of aluminium in arctic environments*. 2013, Institute for Material Science and Technology, NTNU: Trondheim, Norway.
43. Nisancioglu, K., *Electrochemical Behaviour of Aluminum-Base Intermetallics Containing Iron.* Journal of The Electrochemical Society, 1990. **137**(1): p. 69-77.
44. Park, J.O., et al., *Influence of Fe-Rich Intermetallic Inclusions on Pit Initiation on Aluminum Alloys in Aerated NaCl.* Journal of The Electrochemical Society, 1999. **146**(2): p. 517-523.
45. Galvele, J.R., Corrosion Science, 1981. **21**: p. 551.
46. Nisancioglu, K. *Corrosion and protection of aluminum alloys in seawater*. in *EuroCorr 2004*. 12.-16. September 2004. Nice.
47. Eckermann, F., et al., *The influence of MgSi particle reactivity and dissolution processes on corrosion in Al–Mg–Si alloys.* Electrochimica Acta, 2008. **54**(2): p. 844-855.

48. AluMatter. *Corrosion and Corrosion Control*. [cited 2014 22.05]; Available from: http://aluminium.matter.org.uk/content/html/eng/default.asp?catid=177&pageid=2144416642.
49. Dr. Martin P. Smith, C.V., Michael Jacques, *Corrosion of aluminium*. 2004, Elsevier. p. 113-121.
50. *Aluminium: properties and physical metallurgy*, J.E. Hatch, Editor. 1995, ASM: Ohio. p. 297-298.
51. van de Ven, E.P.G.T. and H. Koelmans, *The Cathodic Corrosion of Aluminum.* Journal of The Electrochemical Society, 1976. **123**(1): p. 143-144.
52. Bardal, E., *Korrosjonsprøving - korttidsmetoder. Sammenfattende sluttrapport, del 1. STF16 A77034.* 1977, Korrosjonssenteret, SINTEF, Trondheim.
53. Vargel, C., *Corrosion of Aluminium*. 2004, Amsterdam, The Netherlands: Elsevier.
54. Research, I.o.M. *Forskningsdata*. 2014 [cited 2014 June 19.]; Available from: http://www.imr.no/forskning/forskningsdata/stasjoner/view/initdownload.
55. K.Srinivasa Rao, K.P.R., *Pitting Corrosion of Heat-Treatable Aluminium Alloys and Welds: A Reveiw.* Trans. Indian Inst. Met, 2004. **57**(6): p. 593-610.
56. Ye Ruan, X.M.Q., Wen Biao Gong, *Corrosion Behaviour of 6082-T6 Al Joint Welded with Twin Wire MIG.* Advanced Materials Research, 2011. **418-420**: p. 1368-1374.
57. Fahimpour, V., S.K. Sadrnezhaad, and F. Karimzadeh, *Corrosion behaviour of aluminum 6061 alloy joined by friction stir welding and gas tungsten arc welding methods.* Materials & Design, 2012. **39**(0): p. 329-333.
58. Maggiolino, S. and C. Schmid, *Corrosion resistance in FSW and in MIG welding techniques of AA6XXX.* Journal of Materials Processing Technology, 2008. **197**(1–3): p. 237-240.
59. *ENAW-AlSi1MgMn (ENAW-6082)*. 2009 [cited 2014 June 10th]; Available from: http://www.steelnumber.com/en/steel_alloy_composition_eu.php?name_id=1157.
60. Standard, N., *Execution of steel structures and aluminium structures*, in *Part 3: Technical requirements for aluminium structures*. 2008: NS-EN 1090-3:2008.
61. International, A., *Standard Test Method for Macroetching Metals and Alloys*. 2013, E340 – 13.
62. ImageJ. *Image Processing and Analysis in Java*. Available from: http://imagej.nih.gov/ij/.
63. *Corrosion of metals and alloys - Determination of resistance to intergranular corrosion of solution heat-treatable aluminium alloys*. 1995, *British Standard Institution*: ISO 11846: 1995(E).
64. *Standard Practice for the Preparation of Substitute Ocean Water*. 2003, ASTM International: ASTM D1141 - 98.
65. Blommedal, K., *Corrosion Development in Welded AA6082 Alloys*. 2013, Deparment of material science and technology: NTNU.

Appendix A Welding parameters

In Table A.1 through Table A.6 the welding parameters for all welded flat bars are listed. V = volt, A = ampere, speed = average welding speed in cm/min, time = duration of welding in min:sec.

Table A.1: Welding parameters for 10A

Layer	**1**	**2**	**3**
V	23.8-24.3	25.5-26.0	24.5-25.0
A	238-244	203-212	227-234
Speed	66	48	90
Time	3:03	4:08	

Table A.2: Welding parameters for 10H.

Layer	**1**	**2**	**3**	**4**
V	24.3 – 25.0	24.0 – 25.0	23.8 – 24.8	24.3 – 24.8
A	250 - 260	207 - 213	240 - 250	208 - 214

Table A.3: Welding parameters for 16H

Layer	**1**	**2**	**3**	**4**	**5**	**6**
V	24.5 – 25.5	24.6 – 25.8	25.0 – 25.5	25.0 – 25.5	24.8 – 25.8	25.0 – 25.3
A	257 - 267	245 - 253	225 - 232	226 - 233	260 - 270	224 - 229

Table A.4: Welding parameters for 20H.

Layer	**1**	**2**	**3**	**4**	**5**	**6**
V	23.8 – 25.0	24.8–25.8	24.3–25.3	24.8–25.3	25.0–25.8	25.2–26.3
A	260 - 270	243 - 252	229 - 234	234 - 240	265 - 276	250 - 262
Layer	**7**	**8**				
V	25.5–26.3	24.8 – 25.5				
A	223 - 233	215 - 224				

Table A.5: Welding parameters for 30A.

Layer	**1**	**2**	**3**	**4**	**5**	**6**
V	24.8 – 25.3	26.8 – 27.5	26.0 – 26.5	26.5 – 27.0	24.6 – 25.3	25.3 – 25.8
A	287 - 293	274 - 287	262 - 268	266 - 270	285 - 293	257 – 267
Speed	56	33	82	51	55	59
Time	3:33	6:01	4:26	3:57	3:39	3:23
Layer	**7**	**8**	**9**	**10**	**11**	**12**
V	26.2 – 26.5	25.5 – 26.3	25.8 – 26.3	25.8 – 26.3	25.8 – 26.3	25.8 – 26.3
A	271 - 274	242 - 249	243 - 248	239 - 250	240 - 247	241 - 245
Speed	50	44	53	79	79	79
Time	4:01	4:35	3:46	2:32	2:31	2:31

Table A.6: Welding parameters for 30H.

Layer	**1**	**2**	**3**	**4**	**5**	**6**
V	25.3 – 26.3	25.3 – 26.0	25.3 – 25.5	25.0 – 25.8	24.8 – 25.5	26.0 – 26.5
A	260 - 272	244 - 254	245 - 252	245 - 254	273 - 290	260 - 270
Layer	**7**	**8**	**9**	**10**	**11**	**12**
V	25.3 – 26.0	25.0 – 25.8	24.7 – 25.3	24.8 – 25.5	25.0 – 25.5	24.8 – 25.2
A	282 - 260	252 - 267	228 - 234	222 - 232	226 - 231	225 - 232

Appendix B Temperature curves for weld simulations

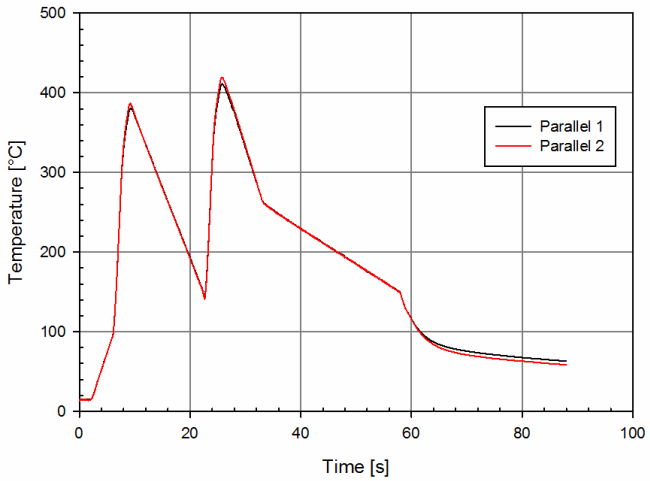

Figure B.1: Temperature curves during weld simulations for the 380-418 samples.

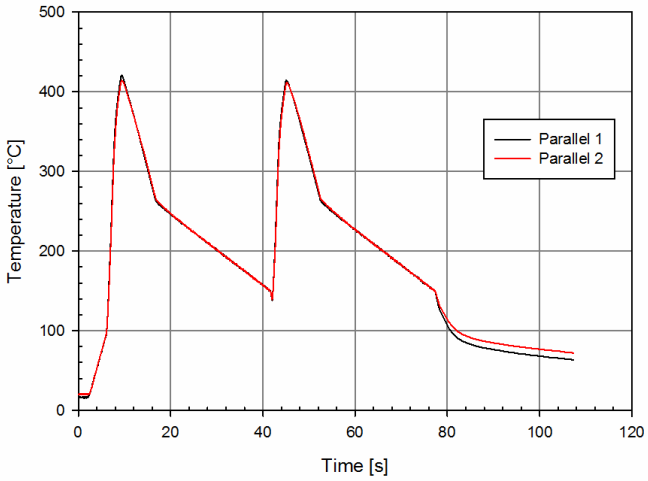

Figure B.2: Temperature curves during weld simulations for the 418-418 samples.

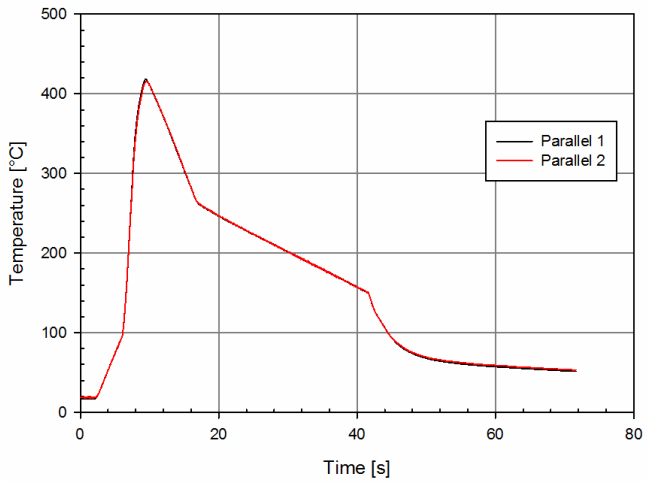

Figure B.3: Temperature curves during weld simulations for the 418 samples.

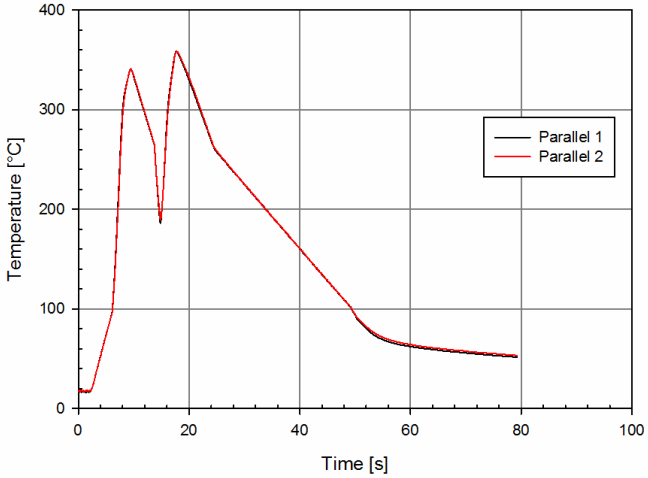

Figure B.4: Temperature curves during weld simulations for the 340-365 samples.

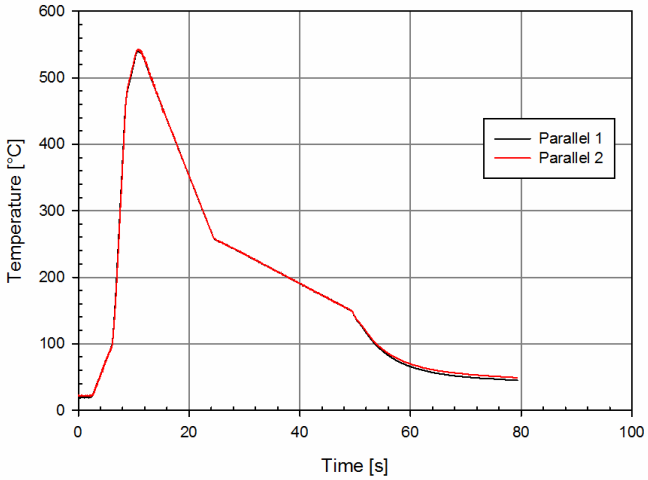

Figure B.5: Temperature curves during weld simulations for the 530 samples.

Appendix C Hardness measurements in welded samples

Table C.1: Hardness measurements in welded samples. HV1: Vickers hardness with 1kg applied load. X: distance from weld center line in mm.

30H		30A		20H		16H		10H		10A	
HV1	x	HV1	x	HV1	x	HV1	x	HV1	x	HV1	x
95	0.0	88	0.0	82	0.0	84	0.0	79	0.0	74	0.0
92	1.0	89	1.0	81	1.0	84	1.0	79	1.0	76	1.0
91	2.0	89	2.0	82	1.9	85	1.9	73	1.9	73	1.9
88	2.9	85	2.9	69	2.9	86	2.9	74	2.8	73	2.9
72	3.9	66	3.9	69	3.8	84	3.9	71	3.8	73	3.9
62	4.8	64	4.9	67	4.8	69	4.9	66	4.7	72	4.9
61	5.7	60	5.9	68	5.8	66	5.9	64	5.7	70	5.8
64	6.7	64	6.8	76	6.8	65	6.9	62	6.7	61	6.7
73	7.7	76	7.8	84	7.8	65	7.8	61	7.7	64	7.8
78	8.7	80	8.8	90	8.8	67	8.8	68	8.6	70	8.7
83	9.7	85	9.8	95	9.7	71	9.8	76	9.6	78	9.7
85	10.7	88	10.7	96	10.7	74	10.7	81	10.5	84	10.6
86	11.7	89	11.7	97	11.7	82	11.7	85	11.5	91	11.6
89	12.7	89	12.7	100	12.6	83	12.7	87	12.5	96	12.6
88	13.7	90	14.7	101	13.6	90	13.7	91	13.5	102	13.5
88	14.6	89	16.7	101	14.6	92	14.7	97	14.4	103	14.5
87	16.6	89	18.7	102	15.6	95	15.7	100	15.3	105	15.5
87	17.7			101	17.6	97	16.7	100	16.3	105	16.4
87	19.7			103	19.7	99	17.6	104	17.3	107	17.4
				103	21.7	103	18.6	105	18.2	107	18.3
						102	19.6	102	19.2	108	19.3
						101	21.6	100	20.2	109	20.3
						101	23.7	101	21.1	111	21.2
						104	25.6	104	22.1	111	22.2
								102	23.1	109	23.3
								107	24.1		
								103	25.0		
								108	26.0		
								109	26.9		
								107	27.9		
								106	28.9		

Appendix D Hardness measurements in weld simulated samples

Table D.1: Hardness measurements in weld simulated samples. HV1: Vickers hardness with 1 kg applied load. x: distance from thermocouples in mm. Sample name indicate peak temperature(s) in heat cycle(s).

380-418		418-418		418		340-365		530	
HV1	x	HV1	x	HV1	x	HV1	x	HV1	x
99	-9.7	101	-12.7	107	-10.2	110	-11.3	65	-13.3
100	-8.7	103	-11.6	103	-9.2	98	-10.3	68	-12.4
101	-7.7	97	-10.6	94	-8.2	107	-9.2	71	-11.4
98	-6.8	96	-9.7	99	-7.2	91	-8.1	74	-10.4
79	-5.8	88	-8.5	88	-6.2	90	-7.0	70	-9.4
84	-4.7	84	-7.5	74	-5.1	84	-6.0	72	-8.3
65	-3.7	76	-6.3	71	-4.2	93	-5.0	71	-7.0
62	-2.7	65	-5.2	64	-3.5	73	-4.0	65	-6.0
56	-1.6	63	-4.1	57	-2.5	75	-3.0	71	-4.9
58	-0.5	60	-3.0	62	-1.4	69	-1.9	74	-3.9
57	0.5	55	-2.0	66	-0.4	68	-0.9	78	-2.8
59	1.6	52	-1.0	61	0.7	60	0.2	81	-1.7
58	2.6	60	0.2	65	1.8	65	1.2	81	-0.7
58	3.6	54	1.2	59	3.0	68	2.2	81	0.5
56	4.6	56	2.2	60	4.0	67	3.2	73	1.6
56	5.6	58	3.3	65	5.1	77	4.2	70	2.7
58	6.5	59	4.4	62	6.1	75	5.4	76	3.8
63	7.6	77	5.5	67	7.1	76	6.4	79	4.9
65	8.7	67	6.5	75	8.2	85	7.5	76	6.0
67	9.8	85	7.6	73	9.2	95	8.5	76	7.0
71	10.8	85	8.7	76	10.2	96	9.5	70	8.1
75	11.8	86	9.7	75	11.2	100	10.5	64	9.1
86	12.8	81	10.8	87	12.2	102	11.5	65	10.2
90	13.8	94	11.7	90	13.3	104	12.6		
95	14.8	104	12.8	86	14.3	107	13.7		
94	15.9	109	14.3	95	15.4				
110	16.9			95	16.4				
110	17.9			103	17.5				
				103	18.5				

Appendix E Electrical conductivity measurements

Table E.1: Electrical conductivity measurements in the base material together with average and standard deviation.

Measurement	10A	10H	16H	20H	30A	30H
1	27.18	28.54	28.42	28.42	29.16	28.8
2	27.06	28.64	28.25	28.39	29.1	28.61
3	27.09	28.34	28.58	28.38	29.06	28.59
Average	**27.11**	**28.50667**	**28.41667**	**28.39667**	**29.10667**	**28.66667**
STD	0.05099	0.124722	0.134743	0.016997	0.041096	0.094634

Table E.2: Electrical conductivity measurements in the HAZ together with average and standard deviation.

Measurement	10A	10H	16H	20H	30A	30H
1	27.67	28.92	28.85	28.67	29.4	29.09
2	27.81	29.01	28.85	28.65	29.49	29
3	27.3	28.77	28.92	28.72	29.26	29.09
Average	**27.59333**	**28.9**	**28.87333**	**28.68**	**29.38333**	**29.06**
STD	0.215149	0.098995	0.032998	0.029439	0.094634	0.042426

Table E.3: Electrical conductivity measurements in the weld material together with average and standard deviation.

Measurement	10A	10H	16H	20H	30A	30H
1	13.82	13.89	13.11	13.23	13.33	12.95
2	14.05	14.14	13.09	13.26	13.31	13.14
3	13.22	14.27	13.13	13.09	13.24	13.13
Average	**13.69667**	**14.1**	**13.11**	**13.19333**	**13.29333**	**13.07333**
STD	0.349889	0.157692	0.01633	0.074087	0.038586	0.087305

Appendix F Particle analysis

This appendix presents the results from the particle analysis and the size distribution of the particles for all examined samples.

Table F.1: Summary of particle analysis for all examined samples.

Sample	Particle type	Density [#particles/mm^2]		Average size [µm]		Area fraction of particles [%]	
		Base	HAZ	Base	HAZ	Base	HAZ
10H	Primary	3248 ± 124	3676 ± 179	1.77 ± 0.0445	1.82 ± 0.0478	0.798 ± 0.0221	0.962 ± 0.0818
16H	Primary	2447 ± 199	2495 ± 301	2.78 ± 0.203	2.36 ± 0.0976	1.48 ± 0.108	1.10 ± 0.208
20H	Primary	1937 ± 67.1	1710 ± 140	2.66 ± 0.138	2.32 ± 0.0601	1.08 ± 0.128	0.718 ± 0.0236
30H	Primary	1844 ± 113	2218 ± 209	2.42 ± 0.0639	2.17 ± 0.0355	0.845 ± 0.0376	0.823 ± 0.0977
10H	Dispersoid	876208 ± 34375	804361 ± 11139	0.188 ± 0.00425	0.176 ± 0.00913	2.44 ± 0.152	1.95 ± 0.165
16H	Dispersoid	913404 ± 91081	856129 ± 109296	0.189 ± 0.00473	0.200 ± 0.00302	2.57 ± 0.157	2.67 ± 0.284
20H	Dispersoid	884342 ± 132765	943042 ± 89924	0.229 ± 0.0189	0.188 ± 0.00425	3.546 ± 0.0732	2.615 ± 0.295
30H	Dispersoid	1276847 ± 62647	940550 ± 52580	0.180 ± 0.00167	0.170 ± 0.00470	3.25 ± 0.0890	2.13 ± 0.197

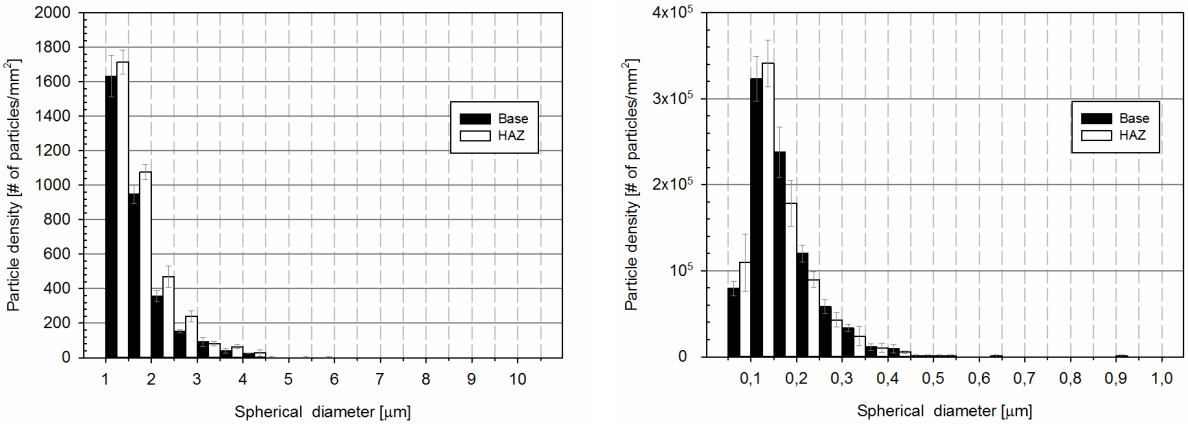

Figure F.1: Size distribution represented as particle density for primary particles (left) and dispersoids (right) for 10H.

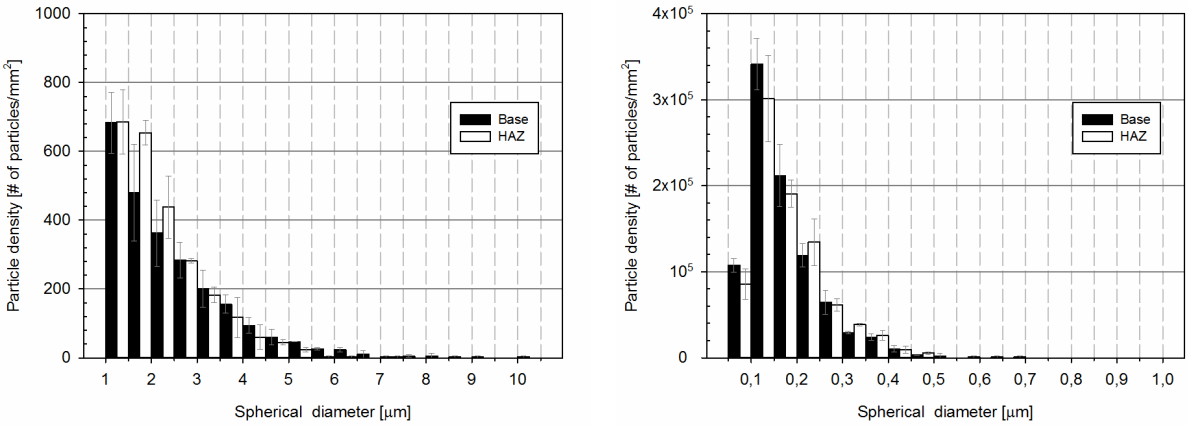

Figure F.2 Size distribution represented as particle density for primary particles (left) and dispersoids (right) for 16H

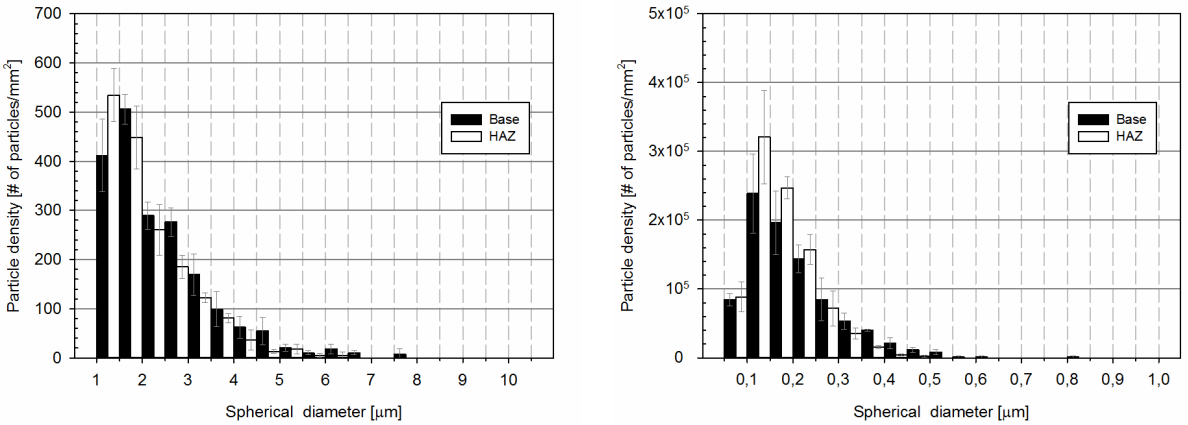

Figure F.3 Size distribution represented as particle density for primary particles (left) and dispersoids (right) for 20H

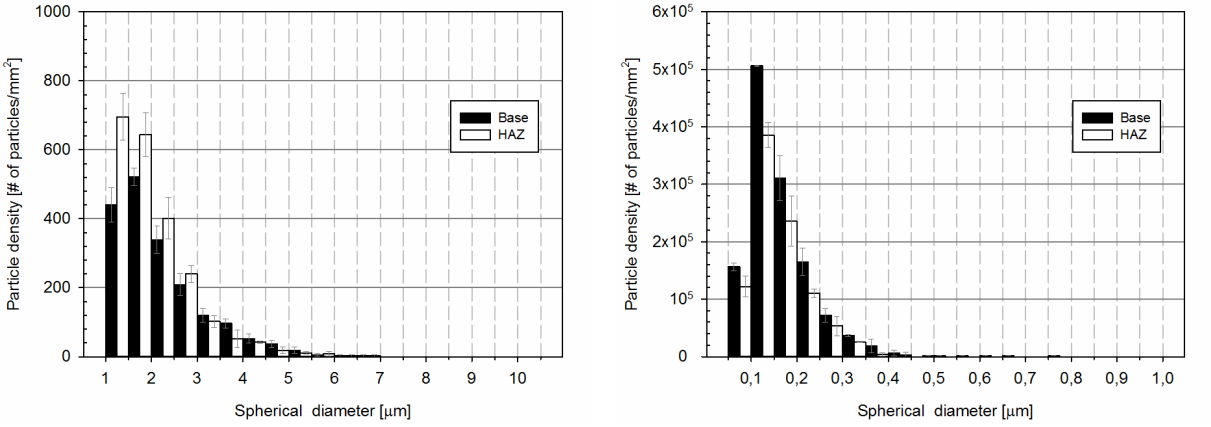

Figure F.4 Size distribution represented as particle density for primary particles (left) and dispersoids (right) for 30H